TIME-RESOLVED TRANSMISSION AND REFLECTIVITY STUDIES OF PULSED-LASER IRRADIATED SILICON-ON-SAPPHIRE

by

MING-CHIH LEE

B. S., Chung Yuan Christian College of
Science and Engineering, 1975

A MASTER'S THESIS

submitted in partial fulfillment of the

requirements for the degree

MASTER OF SCIENCE

Department of Physics

KANSAS STATE UNIVERSITY
Manhattan, Kansas

1982

Approved by:

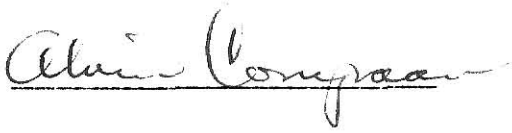

TABLE OF CONTENTS

LIST OF FIGURES

ACKNOWLEDGMENTS

I would like to thank my major advisor, Alvin Compaan, for his guidance, teaching, and patience through the course of this work. Without his assistance, I could not have finished this work.

I also want to thank Nate A. Folland and Tom Gray for serving on my committee.

I would like to acknowledge R. Hodgson and J. Gillaland for generously supplying S.O.S. samples.

I also appreciate the help and friendship of my co-workers, H. W. Lo, and A. Aydinli.

I am grateful for the fine typing by Sheryl Spisak and the fine drawings by Mike Heule.

I am deeply indebted to my wife, Nien-pin, for her encouragement, patience, and love.

The financial support of the U. S. Office of Naval Research under Contract No. N00014-80C-0419 is gratefully acknowledged.

Chapter 1

INTRODUCTION

Ions from ion sources in the KeV to MeV energy range can be accelerated to bombard a solid substrate and thus produce changes in the electrical and optical properties of the material. This is called ion-implantation. This technique has been widely applied and replaces the conventional semiconductor-processing techniques like diffusion and alloy regrowth to manufacture semiconductor devices such as the single P/N junction MOSFET, because it has advantages of low-temperature doping, dose control, and spatial masking. However, there are two major problems in processing semiconductors with this technique.[1] One is the displacement damage in the crystal lattice, the other is that only 10-20% of implanted dopants are electrically active.[2] Fortunately, in 1974 Khaibullin et al.[3] proposed a new method of implanted layer annealing to solve these problems. This method of laser irradiation can remove the lattice defects induced by ion implantation and activate the implanted ions electrically. They called it "laser annealing" in comparison with conventional thermal annealing.

Because laser annealing has advantages over thermal annealing, it appears to be a promising technique in fabrication of devices made from implanted materials. The first advantage is that the laser energy can be absorbed in a very thin surface layer (a few tenths of microns) and produces the necessary conditions for annealing to take place only in the

thin layer. The thick undamaged substrate is not affected by the incident laser energy. The laser annealing can be carried out in air due to the extremely fast recrystallization time (~100 nsec). Therefore, a second advantage is that it avoids a vacuum processing step. (However, this step is still needed for ion-implantation.) A third advantage is its wide range of spatial and temporal selectivity so that we can perform it in a selected area for a controlled duration. These are good conditions for mass production.

Since the advent of laser annealing, many researchers have been interested in it for device applications for the reasons listed above. But, physicists are especially concerned about the mechanism of laser annealing. Different models have been proposed to interpret the mechanism of laser annealing. The strictly thermal melting model[4] and the non-thermal plasma annealing model[5] are two popular models and discussed by most papers.

It is suggested in the thermal melting model that the laser energy is immediately transferred to the lattice (coupling rate $\sim 10^{12}$ sec^{-1}), thus the amorphous layer may melt and recrystallize epitaxially. This model is the most widely accepted because it is simple and can account for many features of CW and pulsed (> 50 nsec) laser annealing. For instance, the enhanced reflectivity during annealing is similar to that of the molten phase.[4] Implanted dopant concentrations after pulsed-laser annealing are higher than the conventional solubility limits. According to Wood,[6] this non-equilibrium process could be caused by melting and ultrarapid recrystallization.

Another piece of evidence often used to support the melting model is the cell structure for some implanted species (such as In^+) in Si which

has been laser-annealed. The average cell size is about 350Å for In^+ -doped Si. The core of the cell is doped single crystal Si while the cell walls are almost pure In^+ dopants. This cell formation starts at 950Å depth with the walls nearly perpendicular to the growing interface. Such features are also orientation dependent.[7] White et al.[8] proposed that it arises from the interfacial instability which develops during re-growth by constitutional supercooling at the liquid-solid interface.

In contrast to the melting model, the non-thermal plasma annealing model suggests that the absorbed laser energy generates dense carriers in the implanted material. This is because the incident photons will excite the electrons from valence to conduction bands and produce a high density of electron-hole pairs in the form of a plasma witin a couple tens of nanoseconds. During such a process, the density gradient of carriers tends to pull more carriers into the so called "self-confined" region due to more available states in this highly excited region. Also the electron-phonon coupling seems to be inhibited and most of the energy is retained in the carriers until the diffusion becomes dominant. When the self-confinement is over, most energy is dissipated by luminescence or interband transitions and heat diffusion. Therefore, the amorphous layer does not have a chance to reach the melting temperature. It looks more complicated but is also a feasible model. However, many details of this model still need to be examined closely.

Although the thermal melting model is most popular and supported by a large number of people, there are certain features in the nanosecond pulse regime the melting model cannot explain. One is the low lattice temperature rise (300 ± 50°C) measured by Compaan and Lo.[9] Since we know

that the melting point of silicon is 1420°C, it contradicts the melting model. Another one is that the thermal melting model cannot explain the behavior of the residual strains of the annealed silicon-on-sapphire.[10] Furthermore, the time-resolved conductivity during laser annealing is much smaller than the value of ordinary molten silicon.[11] By comparing the enchanced reflectivity during pulsed laser annealing with the value for molten silicon, it shows only 2% discrepancy in the perpendicular polarization but 20% in the parallel polarization.[12]

Tsu et al.[13] found that their results of pulse laser annealed Si are not consistent with either a normal melting process or a solid phase epitaxial regrowth. They measured the acoustic wave amplitude due to the thermoelastic expansion in terms of incident energy density. One would expect an abrupt change in amplitude upon the surface density change, because the molten Si is 10% more dense than solid Si. However, they only saw a monotonic change over a wide range of energy density from partial annealing to surface damage. This cannot be explained by the melting process in which the change of Si density occurs. Hoonhout and Saris[14] investigated the result of Baeri et al.'s experiment[15] and found no correlation between the observed dopant redistribution and the normal thermal redistribution coefficient. Hence, segregation cannot be treated as evidence for the melting model. Yoffa[16] calculated that the diffusion rate of the hot, dense carriers can substantially reduce the rate at which energy is transferred to the lattice so that the semiconductor may not reach melting temperature before carrier diffusion spreads energy into the bulk.

In order to clarify the actual mechanism of pulsed laser annealing, we have done a series of experiments involving Time-Resolved Transmission

and Reflectivity of Pulsed-Laser Irradiated Silicon-on-Sapphire.[17] The behavior of reflectivity and transmission will be discussed in the following chapters in three roughly divided time regimes. They are the long-time regime (> 1 μsec), the intermediate time regime (∿100 nsec to 1 μsec), and the high reflectivity phase (0 to 100 nsec).

In Chapter 2, I describe the experimental schemes first. In order to infer the temperature, we have done the transmission measurement of silicon-on-sapphire using a conventional furnace for temperature calibration. The temperature in the long time regime will be inferred from the transmission result by comparing with oven calibration.

In the third chapter, the different features of reflectivity and transmission as probed with CW lasers will be discussed in the intermediate time regime by taking into account the multiple interference effect, sample thickness, and wavelength dependence. We also calculated the multiple reflection and transmission in terms of temperature with the known temperature dependent parameters of absorption coefficient, index of refraction and thermal expansion coefficient. Thus, temperature is inferred from computer simulation during this intermediate time regime.

In the fourth chapter, we will take a close look at the experimental results during the high reflectivity phase, such as the detector response, power dependence, sample thickness dependence and spectral dependence. Then a Kramers-Kronig analysis[18] is applied to interpret the relation between transmission and reflectivity. The transmission during the high reflectivity phase is used to test the melting model.

In the final chapter, there will be a summary of the experiments and our interpretation. We will also point out the unanswered questions and suggest experiments to help understand the physical mechanism of laser annealing.

Chapter 2

TEMPERATURE INFERRED FROM OPTICAL TRANSMISSION IN THE LONG TIME REGIME

In this chapter, I want to discuss the two parts of the experiment in detail. They are the oven-heated and pulsed laser-heated silicon-on-sapphire (S.O.S.). Then, I will compare the results from these two and infer the temperature of the sample.

A. Oven-Heated S.O.S.

As a preliminary experiment, we have performed an optical transmission measurement through a 2 μm thick S.O.S. sample in a conventional tube furnace (Hevi-Duty 70-T) heated from room temperature to 700°C. The experimental apparatus is shown in Figure 1. We have used either a He-Ne laser (633 nm) or an Ar^+ laser (514.5 nm) to irradiate the oven-heated S.O.S. sample. In order to prevent any reaction with the air, we have kept argon gas running through the quartz tube during measurement. The temperature is read out from a Chromel-P-Alumel thermocouple right next to the sample with ice water as reference. The laser power is checked regularly by inserting a calorimeter in the beam. The transmission signal is detected by a solar cell (Edmund Scientific 30538) covered with a light shield. The necessary filters have been selected so that the signal will not saturate the solar cell. By choosing room

Figure 1: Apparatus for measuring the transmission as a function of temperature

L_1 = 33 cm, the oven length

L_2 = 91.5 cm, the quartz tube length.

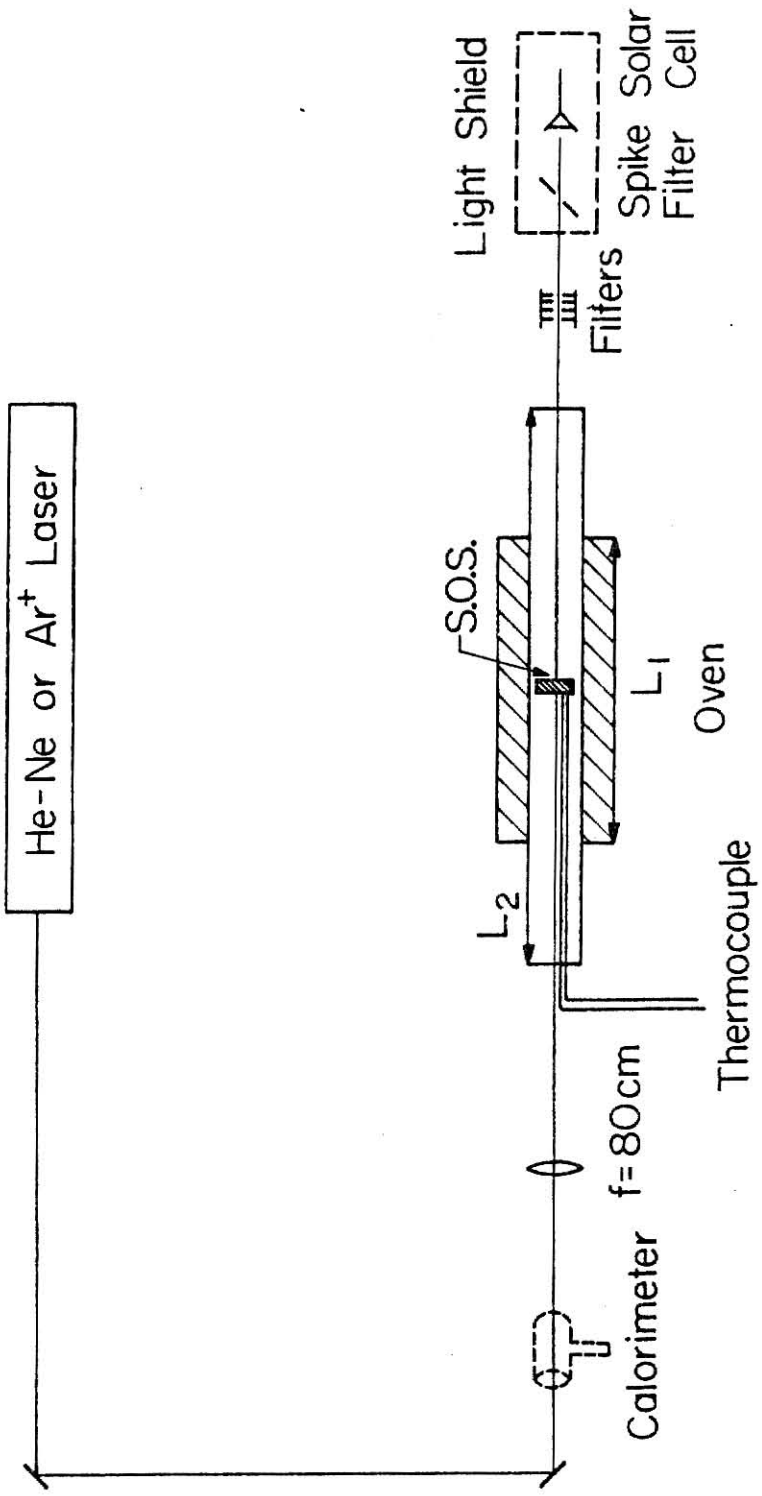
He-Ne or Ar+ Laser
Light Shield
Spike Filter
Solar Cell
Filters
S.O.S.
L1
Oven
L2
Thermocouple
f=80cm
Calorimeter

temperature transmission as unity, we have obtained the transmission ratio as a function of temperature. These data are shown in the upper part of Figure 2. The upper curve is for the probe at 633 nm and the lower one is for 514.5 nm. The 514.5 nm data appear saturated above 400°C. This could be due to a small amount of stray light leaking around the sample which becomes more important as the real transmitted intensity becomes less and less. In fact, recently Jellison et al.[19] have done a measurement of absorption up to 1000°K and found that the transmission ratio at 514.5 nm decreases monotonically with respect to temperature. By including this information, we are able to extend our calibration further. This is shown in the lower part of Figure 2 in a form of calculated absorption coefficient ($\alpha = \frac{1}{z} \ln (\frac{I_{TO}}{I_T})$). The solid lines are just drawn through the data points which show an exponential function of temperature consistent with Jellison's results (refer to p. 31). Thus, the lattice temperature of the sample as a function of time can be inferred by comparing the time-resolved transmission ratio of pulsed laser-heated S.O.S. with that of the calibration.

B. Pulsed Laser-Heated S.O.S.

The experimental apparatus for the time-resolved measurement of pulsed laser-heated S.O.S. is shown in Figure 3. We have used a CW Ar^+ laser (Control Laser 554A) at 514.5 nm and a He-Ne laser (Spectra Physics 125) at 633 and 1152 nm consecutively as probes while using a home-made dye laser pumped by a N_2 laser (Molectron UV 1000) as excitation. Later we also used a second dye laser (Molectron DL-200) pumped by the same N_2 laser as a probe in order to obtain a wider dynamic range and the spectral dependence of the transmission (discussed in chapter 4). Very recently we have used a frequency-doubled Nd:YAG laser (Quanta Ray DCR-1) as a second

Figure 2: Transmission ratio plotted as a function of temperature with room temperature transmission as unity. (Upper part.)

Calculated absorption coefficients as a function of temperature. (Lower part.)

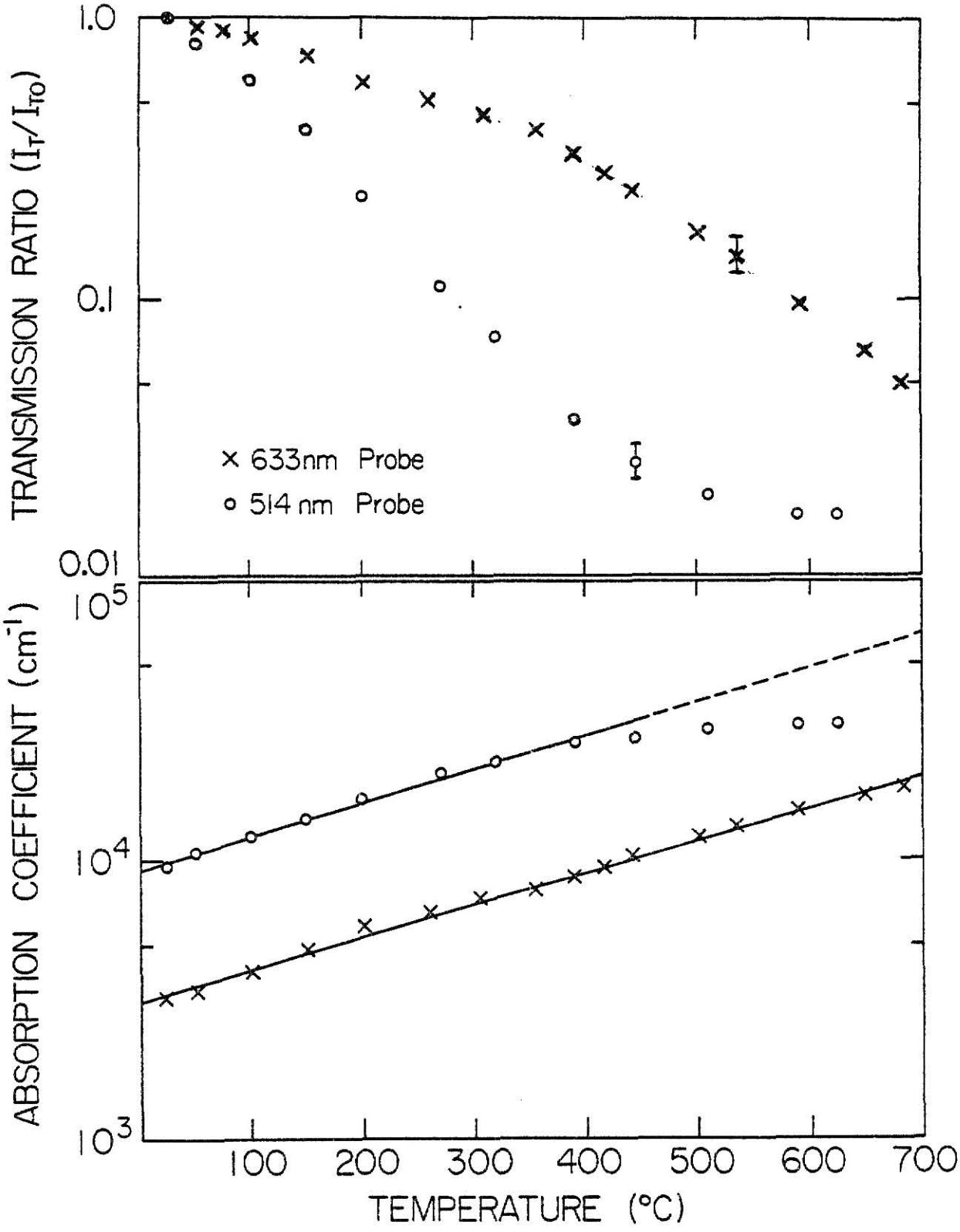
1.0
0.1
0.01
TRANSMISSION RATIO (I_T/I_{TO})
× 633nm Probe
o 514 nm Probe
10^5
10^4
10^3
ABSORPTION COEFFICIENT (cm^{-1})
100
200
300
400
500
600
700
TEMPERATURE (°C)

Figure 3: Apparatus for measuring the reflectivity and transmission of pulsed laser-heated sample. Spatial filter is in the dashed square.
f_1 = 30.8 cm, f_2 = 36.4 cm, f_3 = 5.1 cm

f_4 = 25.4 cm, f_5 = 15 cm, f_6 = 100 cm

f_7 = 19.8 cm, f_8 = 12.6 cm, L = 230 cm.

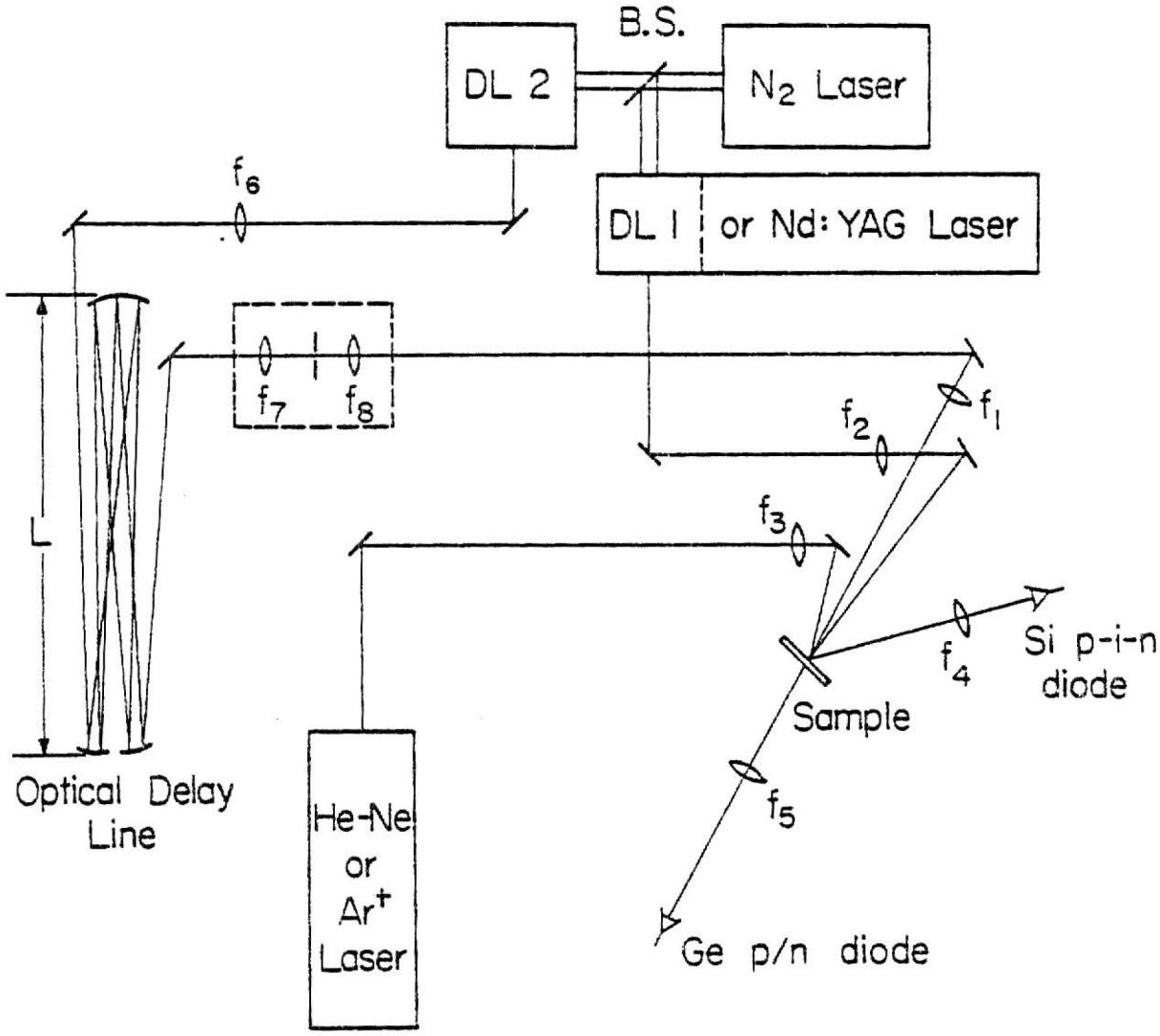
B.S.
DL 2
N_2 Laser
f_6
DL 1
or Nd: YAG Laser
f_7
f_8
f_1
f_2
f_3
L
f_4
Si p-i-n diode
Sample
f_5
Optical Delay Line
He-Ne or Ar^+ Laser
Ge p/n diode

excitation source to see if there is any effect due to excitation frequency and to look for any effect due to the small spot size of the dye laser. (See Chapter 3.)

Appropriate high speed detectors (rise time ~5 nsec) were chosen for receiving the probe signal of different wavelength, for instance a Ge P/N diode (Judson J-16) for 1152 nm and a Si PIN diode (HP 2-4220) for 514.5 nm and 633 nm. In some cases, we used an RCA 1P28 photomultiplier to detect extremely weak signals. All the signals were displayed on a Tektronix 7904 oscilloscope and photographed with Polaroid type 410 film.

The beam overlap of both probe and excitation was checked repeatedly with 50 μm pinhole placed at the same position as the sample. The angles of incidence for excitation and probe beams are smaller than 10^{o} with respect to the normal of the sample. By translating the pinhole vertically and horizontally, we know that both beams are fairly circular. With the measured transmission ratio of each beam through the 50 μm pinhole and assuming circular beams, the calculated probe size is 55 ± 5 μm and that of excitation is 220 ± 40 μm. We also checked the homogeneity of the excitation beam and found no hot spot. Since the signal is sensitive to the light leakage around such a small area, we tried defocusing the probe size by a factor of two and saw no significant change in transmission. This makes us believe that the minimum transmission is not limited by the experimental geometry. By inserting the proper filters in the beam, the power density of the excitation pulse was adjusted well above the annealing threshold ($\geq$ 0.5 J/cm^2) but below the damage threshold (~1.5 J/cm^2) so that we are able to see the enhanced reflectivity (80 to 100 nsec) and reduced transmission.

We have obtained the temporal dependence of transmission at 514.5

and 633 nm as shown in Figure 4. Because all the transmission traces are so similar and reproducible on the samples of different thickness (> 0.07 μm), we chose the transmission trace of 1.16 μm thick S.O.S. for its clarity to calculate the transmission ratio. By taking into account the difference due to the samples of different thickness, we can infer the temperature evolution of S.O.S. after the excitation pulse as shown in Figure 5. From this figure, we obtained some idea about the crystal temperature during laser annealing. Both the 514.5 and 633 nm probes show very consistent temperature beyond 1 μsec, so we might infer that the thermal equilibrium has been completely reached throughout the Si thickness and the lattice temperature is about 250°C. During the time regime shorter than 1 μsec, the data points start to separate by 100°C or less from 633 to 514.5 nm probes. This could be due to the error of using the extrapolated absorption coefficient for 514.5 nm probe. However, it is still good for inferring the temperature with only 100°C uncertainty. This is in good agreement with the result of Lo and Compaan by Raman Stokes-anti-Stokes techniques.

Figure 4: Transmission curves taken from 1.16 μm S.O.S. sample excited by a 485 nm pulse ($\sim$ 0.9 J/cm^2).

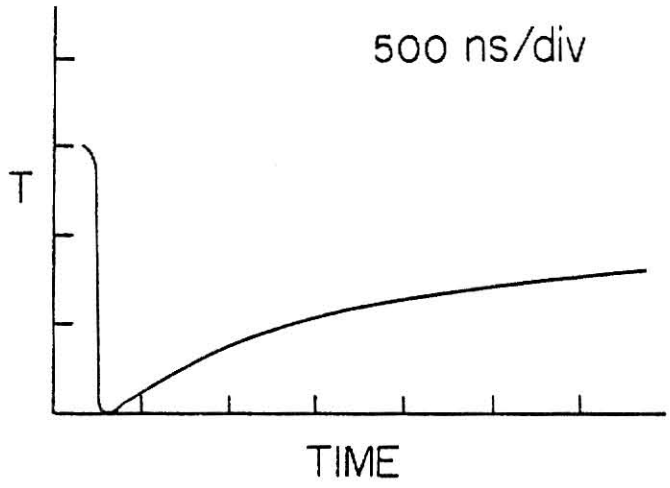

λ_p = 514.5 nm

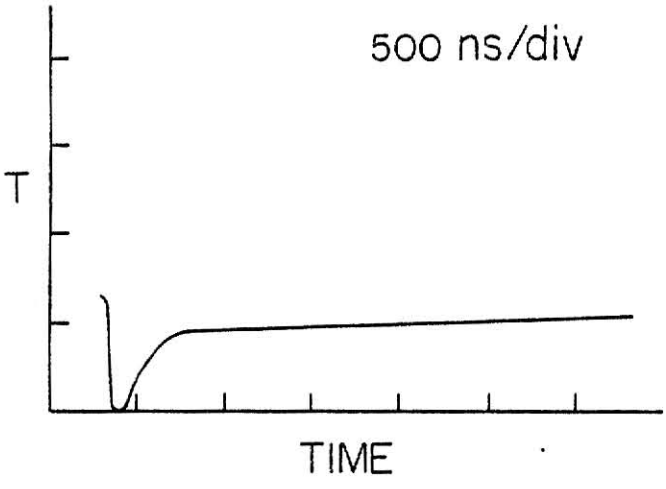

λ_p= 633 nm

Figure 5: Temperature deduced from the Figure 4 using the oven-calibration curve.

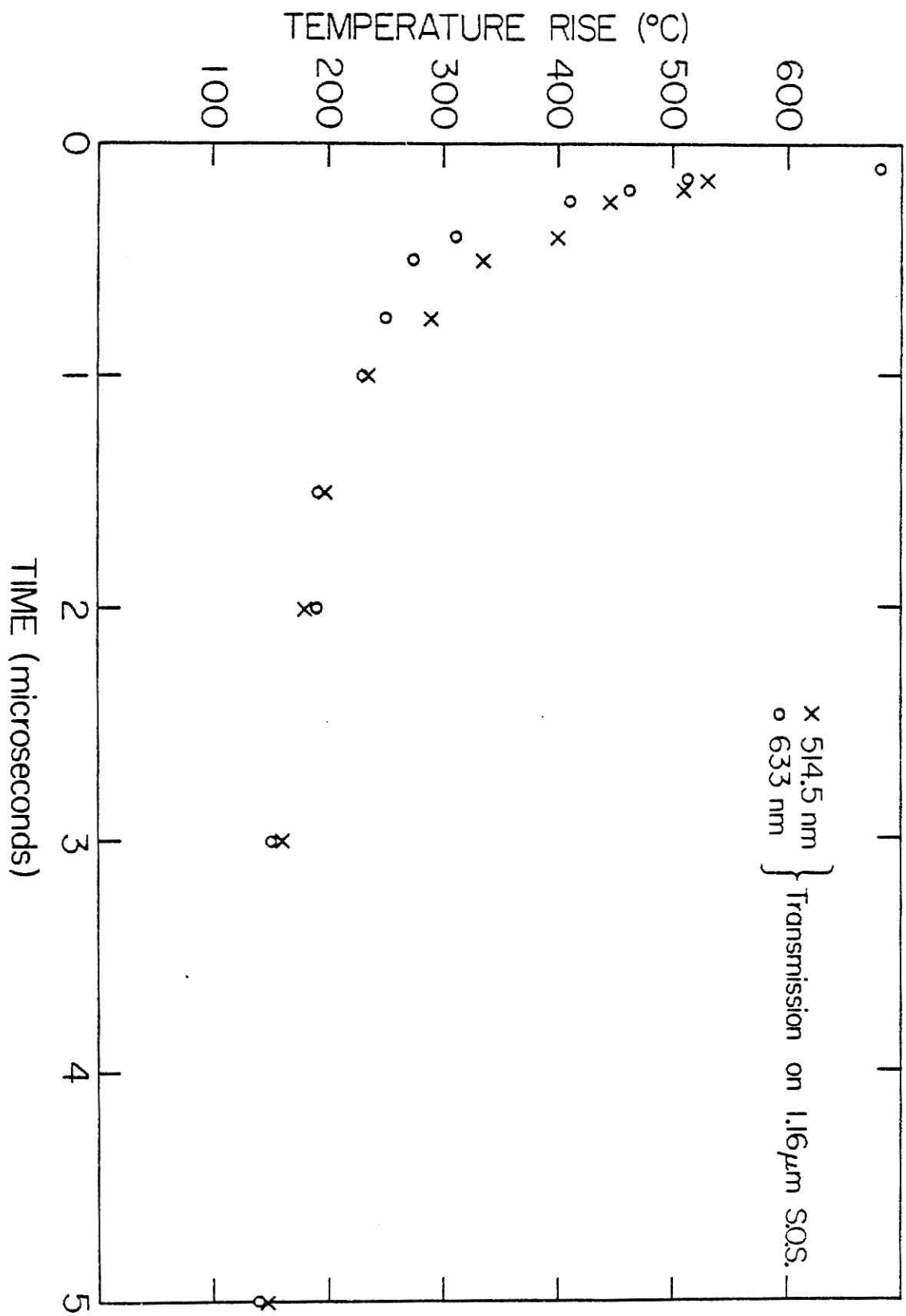
TEMPERATURE RISE (°C)
100
200
300
400
500
600
0
1
2
3
4
5
TIME (microseconds)
× 514.5 nm
o 633 nm
} Transmission on 1.16μm S.O.S.

Chapter 3

REFLECTIVITY AND TRANSMISSION IN THE INTERMEDIATE TIME REGIME -- MULTIPLE INTERFERENCE

A. Experimental Data

We have discussed the features beyond 1 μsec. It appears that the electronic system and lattice are thermalized by that time. What about the behavior in the period less than 1 μsec? In Figures 6 (a,b,c), the transmission and reflectivity measurements are taken from a 2 μm thick S.O.S. sample with 1152, 633, and 514.5 nm probes respectively. The traces on a large time scale (200 nsec/div. to 2 μsec/div.) are shown on the right-hand side and those on a short-time scale (50 nsec/div.) are shown on the left-hand side. In all reflectivity curves, we can see clearly an enhanced portion (~70 nsec) and the one probed with 1152 nm has a decreased portion which goes below the initial value right after an enhanced portion. We call this "undershoot." We also see the consistent drop (approximately to zero in 633 and 514.5 nm probes) during the enhanced reflectivity period in all transmission curves. However, the one probed with 1152 nm has an increased portion after the transmission drop. We call this "overshoot."

In Figures 7 (a,b,c), all the measurements are taken from a 1.16 μm thick S.O.S. sample using the same probes as in Figures 6 (a,b,c) with

Figure 6: Reflectivity and transmission data taken from 2 μm S.O.S. sample with three different probes.

(a) 1152 nm, (b) 633 nm, (c) 514.5 nm

Excitation is 485 nm pulse ($\sim$1 J/cm^2).

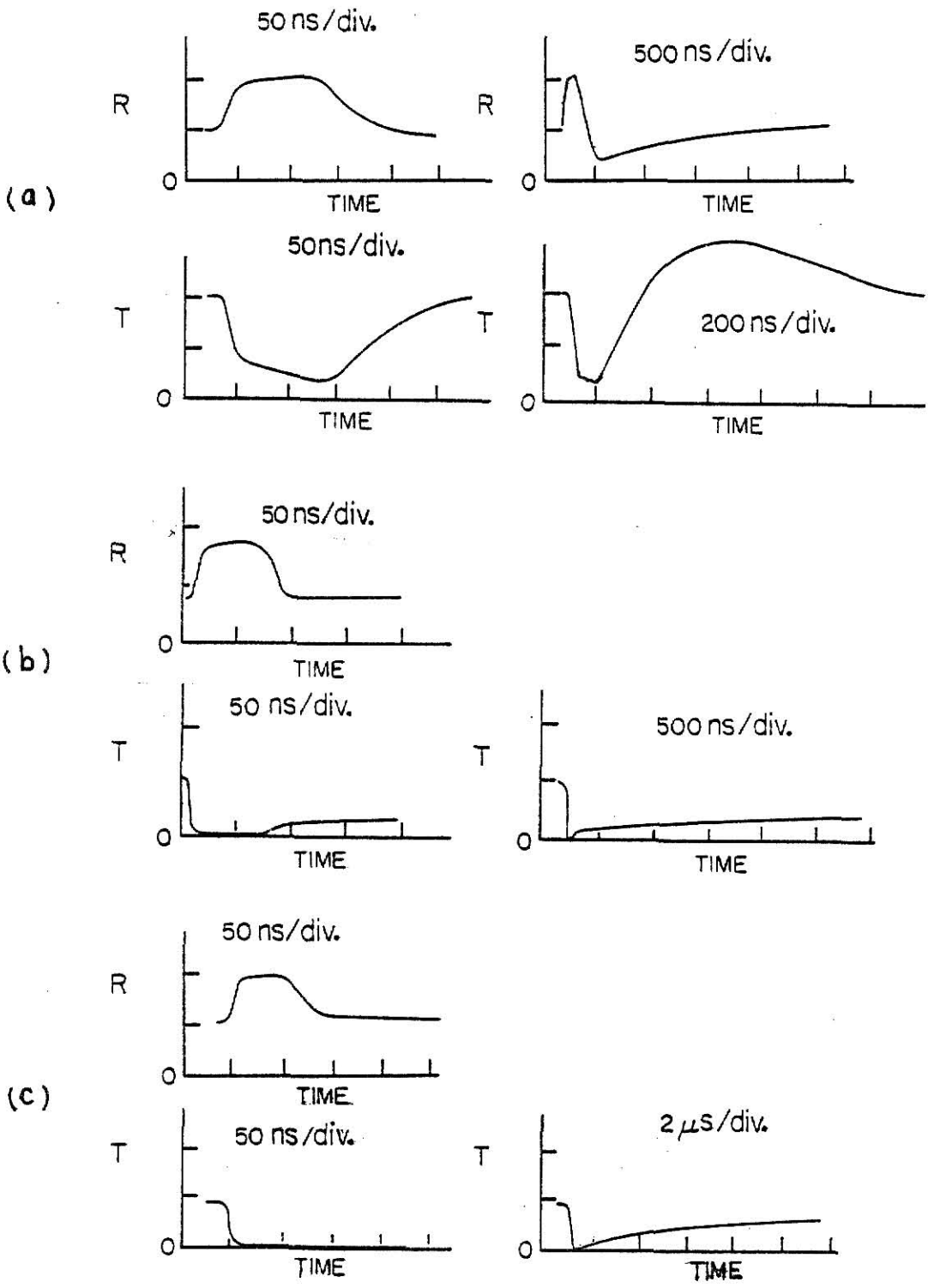
(a)
50 ns/div.
R
0
TIME
500 ns/div.
R
0
TIME
50ns/div.
T
0
TIME
200 ns/div.
T
0
TIME
(b)
50 ns/div.
R
0
TIME
50 ns/div.
T
0
TIME
500 ns/div.
T
0
TIME
(c)
50 ns/div.
R
0
TIME
50 ns/div.
T
0
TIME
2 μs/div.
T
0
TIME

Figure 7: Reflectivity and transmission data taken from 1.16 μm S.O.S. sample with three different probes.

(a) 1152 nm, (b) 633 nm, (c) 514.5 nm

Excitation is 485 nm pulse ($\sim$0.9 J/cm^2).

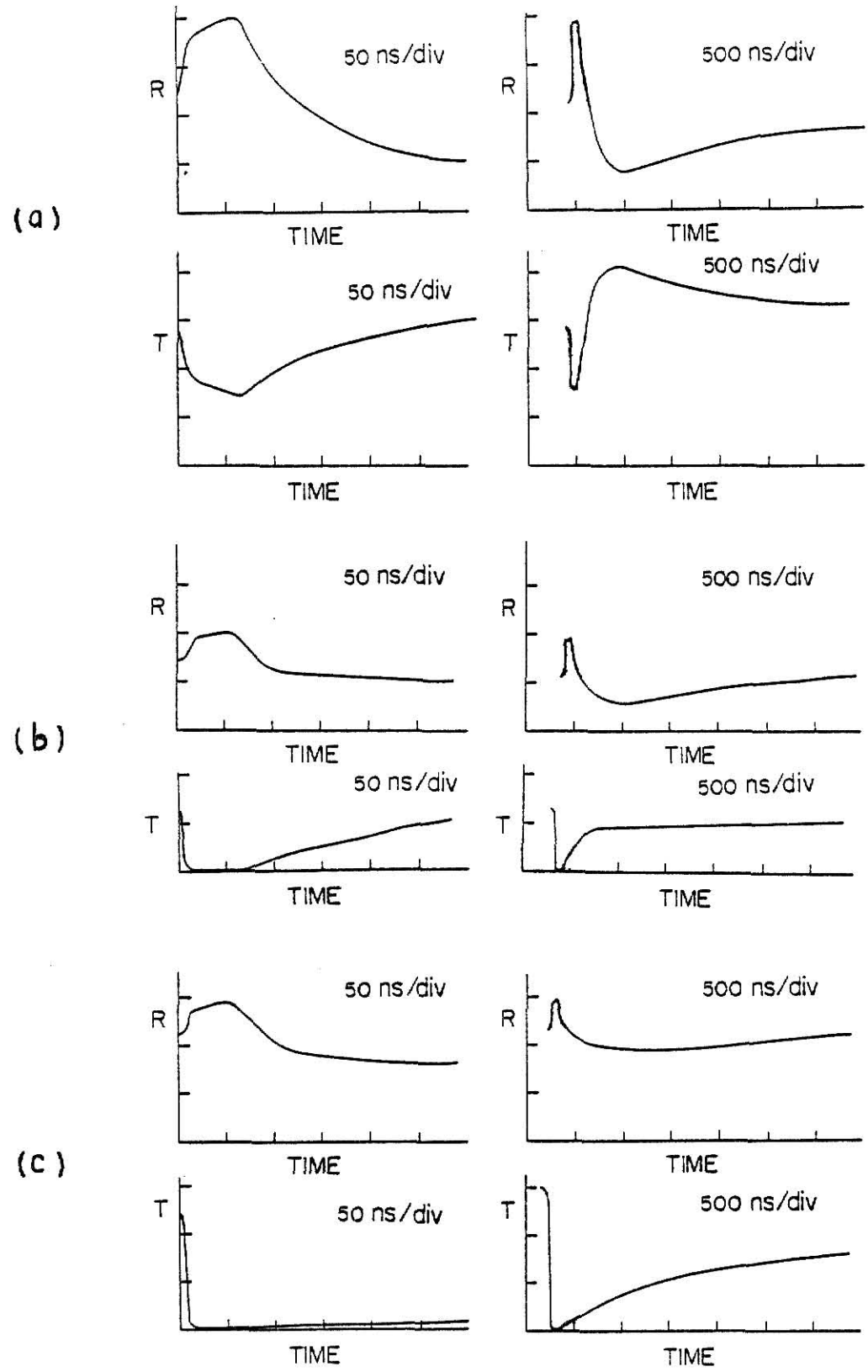
(a)
R
50 ns/div
TIME
R
500 ns/div
TIME
T
50 ns/div
TIME
T
500 ns/div
TIME
(b)
R
50 ns/div
TIME
R
500 ns/div
TIME
T
50 ns/div
TIME
T
500 ns/div
TIME
(c)
R
50 ns/div
TIME
R
500 ns/div
TIME
T
50 ns/div
TIME
T
500 ns/div
TIME

slight variations in excitation power. Again the traces on a short-time scale (50 nsec/div.) are shown on the left-hand side and those on a long-time scale (500 nsec/div.) are shown on the right-hand side. In addition to the enhanced reflectivity, all three probes show the undershoot right after the enhanced portion. Again the transmission curves show a complementary drop and appear to be zero during the enhanced reflectivity period except with the 1152 nm probe.

In Figures 8 (a,b,c), all the conditions are the same as in Figures 7 (a,b,c) but with a 0.6 μm thick S.O.S. The duration of enhanced reflectivity is about the same as in other samples. The reflectivity undershoot is present in 1152 and 633 nm probes, but it is distorted in 514.5 nm probe. However, the transmission overshoot still can be seen only in 1152 nm probe as in Figures 6 and 7.

In order to discuss the reflectivity and transmission traces of Figures 6, 7, and 8 in detail, we have done very careful measurements and found that the multiple interference is an important effect after the enhanced reflectivity portion. Thus we want to concentrate our discussion on the intermediate regime in this chapter. The overshoot and undershoot in this time regime are shown to be the result of an interference effect. The reason that we attribute this behavior to a multiple interference effect is explained as follows. In Figure 9 (a), we probe the reflectivity with 633 nm while exciting the 1.83 μm sample by 485 nm beam of similar energy density for obtaining the data in Figures 6 (b), 7 (b), and 8 (b). Two extreme cases are presented by translating the sample from one side to the other. One has the maximum reflectivity value initially, the other has the minimum reflectivity value initially. This arises from the fact that the sample is not uniform. However, we start

Figure 8: Reflectivity and transmission taken from 0.6 μm S.O.S. sample with three different probes.

(a) 1152 nm, (b) 633 nm, (c) 514.5 nm

Excitation is 485 nm pulse ($\sim$0.9 J/cm^2).

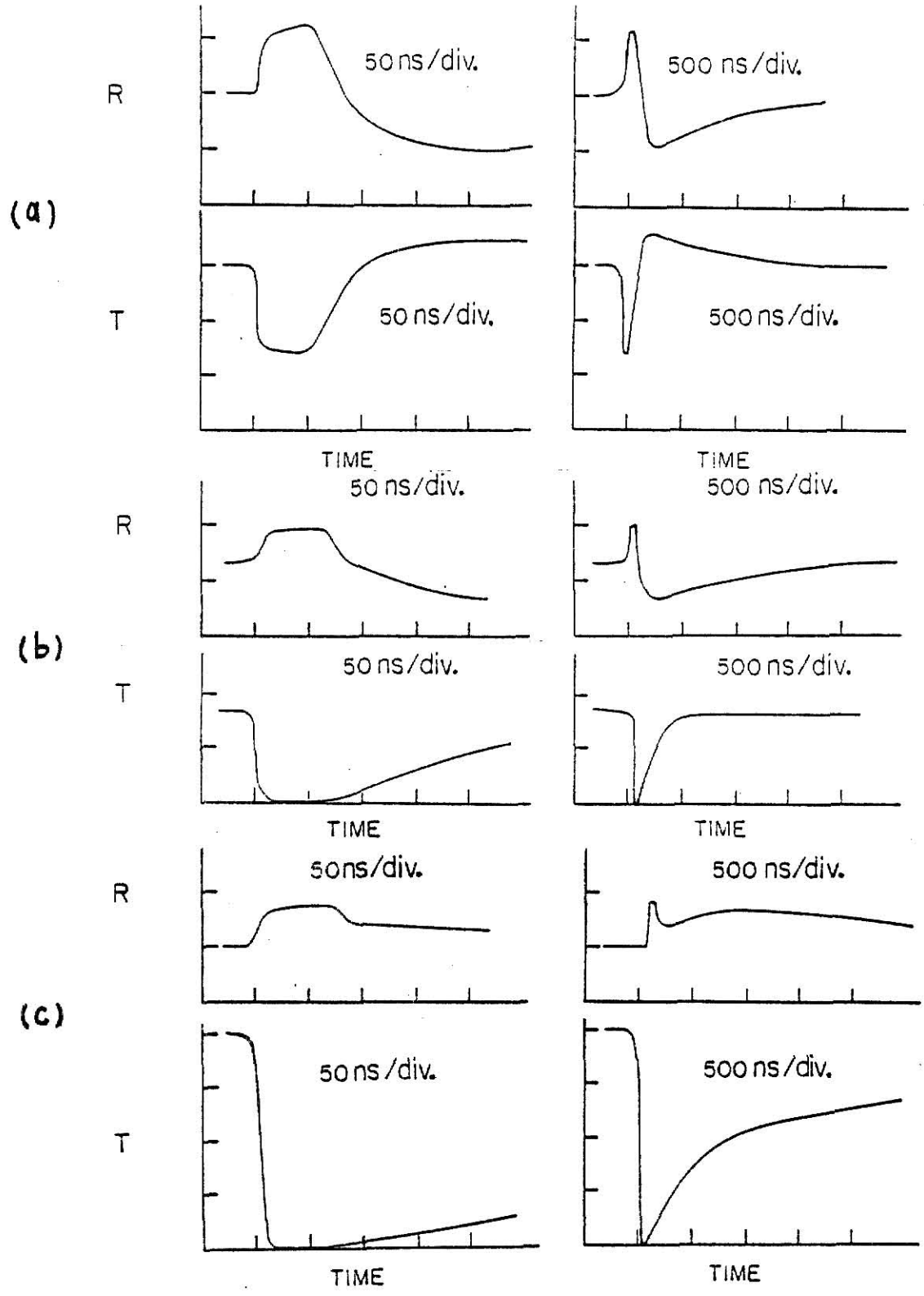
(a)
R
50 ns/div.
500 ns/div.
T
50 ns/div.
500 ns/div.
TIME
TIME
(b)
R
50 ns/div.
500 ns/div.
T
50 ns/div.
500 ns/div.
TIME
TIME
(c)
R
50ns/div.
500 ns/div.
T
50 ns/div.
500 ns/div.
TIME
TIME

Figure 9: Multiple interference effect is shown clearly in reflectivity probed with 633 nm,

(a) on 1.83 μm S.O.S. excited by 485 nm pulse

(b) on 1.83 μm S.O.S. excited by 532 nm pulse (points 2, 3, and 4 correspond to the temperature of 200, 375, and 500°C respectively)

(c) on 0.6 μm S.O.S. excited by 532 nm pulse

All reflectivity curves show approximately the same period of the high reflectivity phase.

(d) on 0.6 μm S.O.S. probed with 514.5 nm

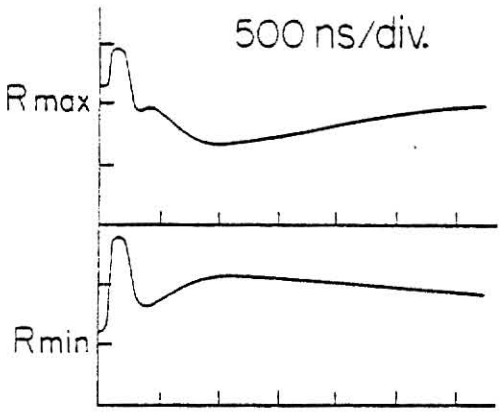

λ_{EX}= 485 nm
(1.83 μm S.O.S.)
(a)

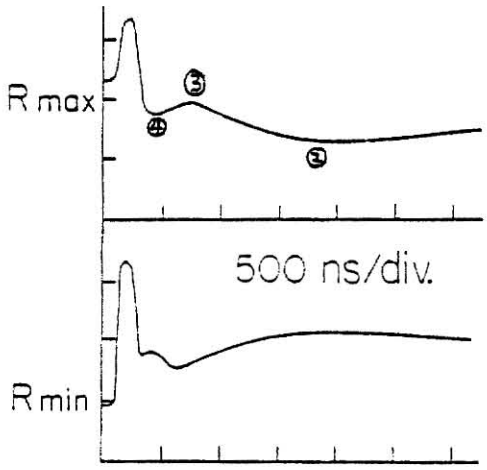

λ_{EX}= 532 nm
(1.83 μm S.O.S.)
(b)

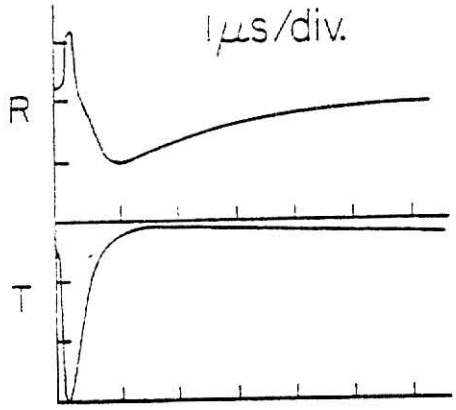

λ_{EX}= 532 nm
(0.6 μm S.O.S.)
(c)

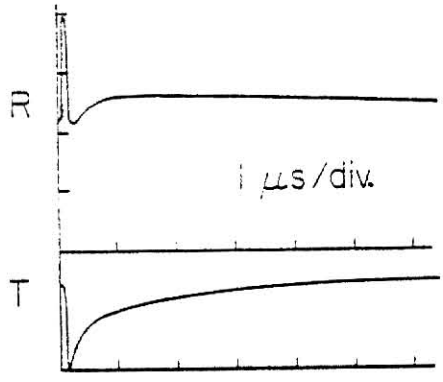

λ_{EX}= 532 nm
λ_p = 514.5 nm
0.6 μm S.O.S.
(d)

to see the oscillations right after the high reflectivity phase. These oscillations will be shown later to infer the temperature.

We also want to see if there is any effect due to the excitation wavelength. This is shown in Figure 9 (b) with the same probe but 532 nm excitation beam. When we keep the duration of the high reflectivity period of Figure 9 (a) and Figure 9 (b) as close as possible so that the conditions are very much alike for both cases, we find no significant difference between them. Thus we conclude that the excitation wavelength does not affect our result much.

There is another factor that can change the experimental results, this is the sample thickness which is shown in Figure 9 (c). All conditions are the same for taking Figure 9 (b) except one with 1.83 μm and the other with 0.6 μm S.O.S. When translating the sample from side to side, we find very few variations in thickness of the 0.6 μm sample, therefore there is no R_{max} or R_{min} initially in Figure 9 (c). However, there is only one-half oscillation after the high reflectivity phase. This agrees with the interference equation ($2d \Delta n = \Delta m\lambda$). The 1.83 μm sample is approximately three times thick as the 0.6 μm sample so that it has three times as many oscillations. As one goes from one maximum to the next minimum or vice versa, $2d \Delta n$ changes by $\frac{1}{2}\lambda$. Knowing the sample thickness, we can obtain the change in refractive index. These multiple interference effects are analyzed quantitatively in the following section.

B. Computer Simulation

Since we want to know the temperature rise during the intermediate time regime, we should find out all the parameters which are temperature dependent. Murakami et al.[20] has measured the index of refraction at 633 nm

to be a linear function of temperature. Weakliem et al.[20] has obtained a similar relationship at 514.5 nm.

$$n(T) = 3.85 + 4.7 \times 10^{-4}\ T(^{\circ}C) \qquad \text{at 633 nm}$$

$$n(T) = 4.2 + 5.46 \times 10^{-4}\ T(^{\circ}C) \qquad \text{at 514.5 nm}$$

We have replaced 3.98 of Ref. 20 by 3.85 to agree with the literature data. The thermal expansion of the sample is also a factor which needs to be considered. Assuming a linear expansion under pulse laser heating,

$$z(T) = z_o\ (1 + \beta\ T)\ ,$$

where z_o is the thickness at room temperature and β is the thermal expansion coefficient. However, this expansion coefficient had been measured by Ibach et al.[21] to be 2.5×10^{-6} at room temperature and increasing to 4.0×10^{-6} at 560°C. Anyway, this is small compared to the temperature coefficient of the refractive index as mentioned above. Thus we have neglected such a small change in thickness while doing the calculation. Another temperature dependent factor is the absorption coefficient which we know from our earlier oven calibration of transmission. We found that it is an exponential function of temperature.

$$\alpha(T) = \alpha_o\ EXP(cT)\ ,$$

where $\alpha_o = 3.2 \times 10^3\ cm^{-1}$ and $c = 2.58 \times 10^{-3}\ ^{\circ}C^{-1}$ at 633 nm and $\alpha_o = 9 \times 10^3\ cm^{-1}$ and $c = 2.8 \times 10^{-3}\ ^{\circ}C^{-1}$ at 514.5 nm.[22] In Figure 10, a simple diagram is sketched to show the multiple reflection and transmission. The little r & t are the amplitude coefficients and the capital R & T are

Figure 10: The simple diagram illustrates the multiple reflection due to the light traveling back and forth between interfaces. In our calculation, the third interface is ignored.

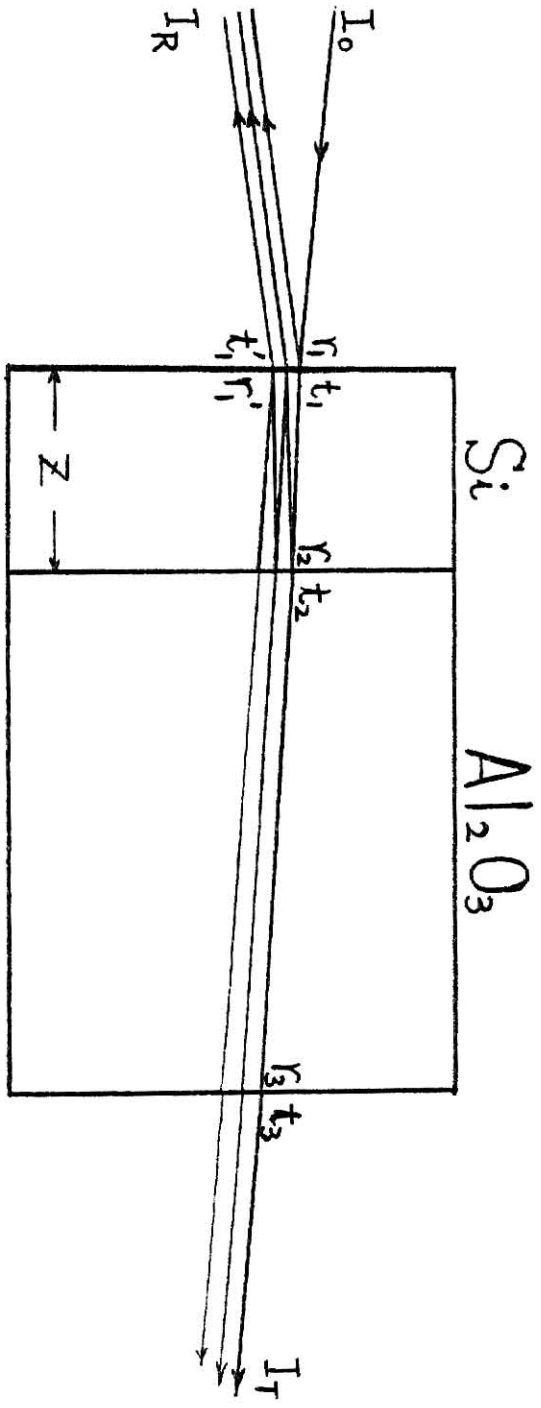
I_R
I_o
r_1
t_1'
t_1
r_1'
Z
Si
r_2
t_2
Al_2O_3
r_3
t_3
I_T

the intensity coefficients. Because the reflection at sapphire-air interface is much smaller than that at the Si-sapphire interface, we ignore the third interface and approximate both the multiple reflection and transmission equations as follows:

$$R = \frac{I_R}{I_o} = r^* r \simeq \frac{1}{X} [r_1^2 + r_2^2 (r_1 r_1' + t_1 t_1')^2 e^{-2\alpha z}$$

$$- 2r_1 r_2 (r_1 r_1' + t_1 t_1') e^{-\alpha z} \cos\delta]$$

$$T = \frac{I_T}{I_0} = t^* t \simeq \frac{1}{X} (t_1^2 t_2^2 e^{-\alpha z})$$

$$X = 1 + r_1'^2 r_2^2 e^{-2\alpha z} - 2r_1' r_2 e^{-\alpha z} \cos\delta$$

$$\delta = 2knz \cos\theta_t \quad .$$

For $\theta_t = 0^o$,

$$\delta \simeq 4 \pi nz/\lambda$$

$$r_{\theta \simeq 0} \simeq \frac{n_t - n_i}{n_t + n_i} \quad , \qquad t_{\theta \simeq 0} \simeq \frac{2n_i}{n_t + n_i} \quad .$$

Since we know that the absorption coefficient, index of refraction and sample thickness are functions of temperature under thermal equilibrium conditions, we used a computer simulation to calculate the multiple reflection and transmission in terms of temperature. By adjusting the parameter z slightly, we can obtain R_{min} or R_{max} value initially.

The results are shown in Figure 11 (a,b,c). Computer programs are in Appendices.

C. Temperature Inferred From Computer Simulation

Because the experimental results show the reflectivity and transmission in terms of time, we need to make a one to one correspondence by matching the relative maxima and minima. It is clear that beyond several tens of μsec the sample is thermalized to room temperature because we do not see any more oscillations at all. Since we have an initial R_{max} value in the upper curve of Figure 9 (b), the final value should be R_{max} too and it corresponds to room temperature. As one moves closer to the high reflectivity phase, one will pass points 2, 3, and 4 which relate to the temperature of 200, 375, and 500°C respectively, as shown in Figure 11 (a). Similarly, when one starts at the R_{min} initial value in the lower curve of Figure 9 (b), one can get another set of temperatures from Figure 11 (b). Thus the temperature evolution can be deduced from the reflectivity data as shown in Figure 12.

An alternative way to infer the temperature as we mentioned earlier in chapter 2 is the transmission ratio which had been calibrated in the furnace and explained in chapter 2. The results from different samples and probes are also shown in Figure 12 and in good agreement with the results from the reflectivity data.

There is a significant difference between 0.6 and 1.83 μm samples. Because the absorption length for the 532 nm excitation pulse is 1.2 μm, the 0.6 μm sample absorbs about half the total incident energy but the 1.83 μm sample absorbs almost the total energy. However, the 1.83 μm sample is three times as thick as the 0.6 μm sample for dissipating the energy. So after the heat diffusion into the bulk, we would

Figure 11: Computer simulation of reflectivity (solid curves) and transmission (dotted curves) in terms of temperature with a 633 nm probe (a,b)

(a) on 1.83 μm S.O.S. with initial R_{max} value,

(b) on 1.83 μm S.O.S. with initial R_{min} value,

(c) on 0.6 μm S.O.S. with approximately R_{min} initial value. (514.5 nm probe)

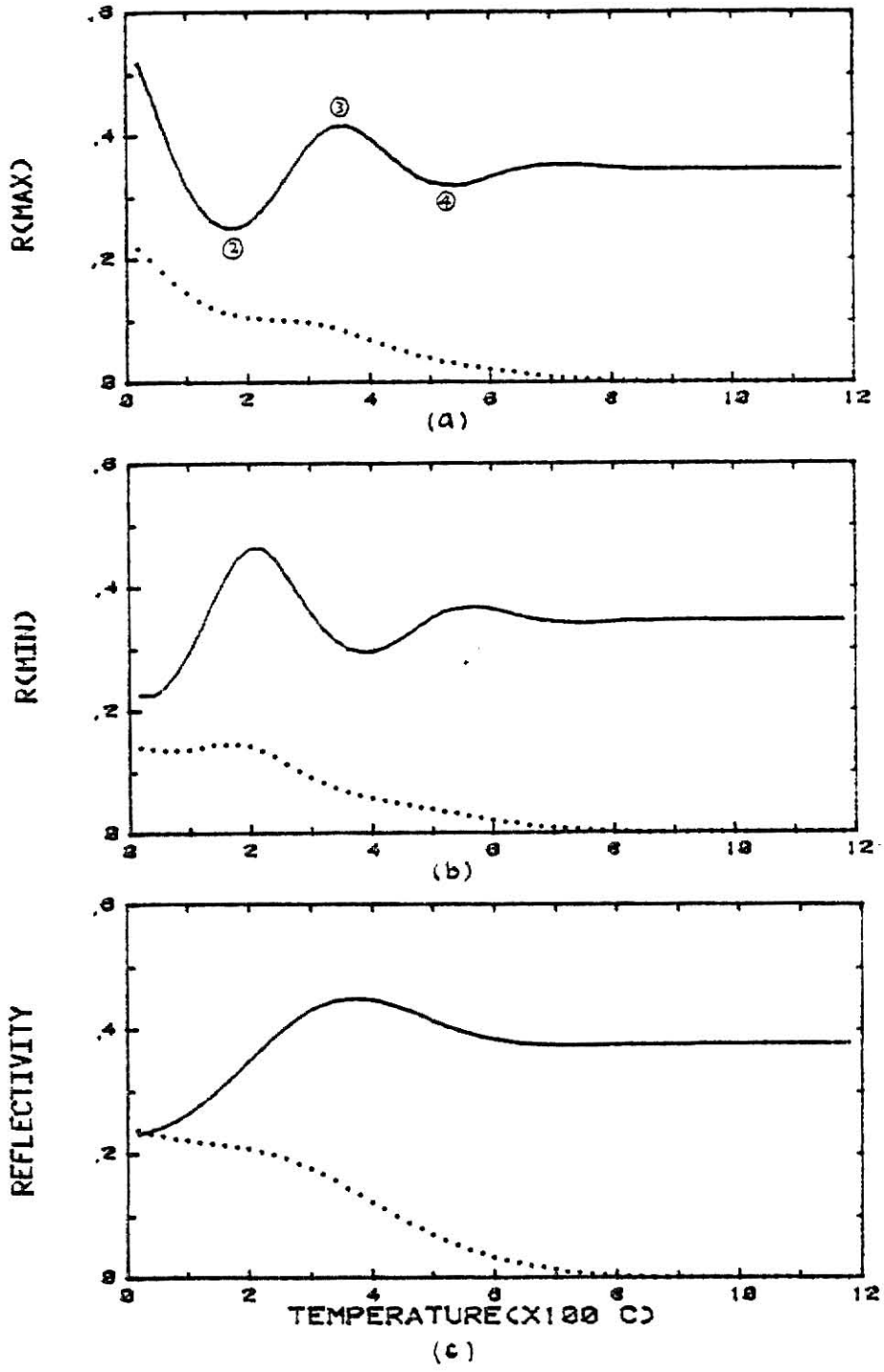
R(MAX)
R(MIN)
REFLECTIVITY
TEMPERATURE(X100 C)
(a)
(b)
(c)

Figure 12: Temperature evolution inferred from the reflectivity and transmission data of different samples and probes. The solid curves are just drawn through the data points. The upper one is for 0.6 μm S.O.S. The lower one is for 1.83 μm S.O.S.

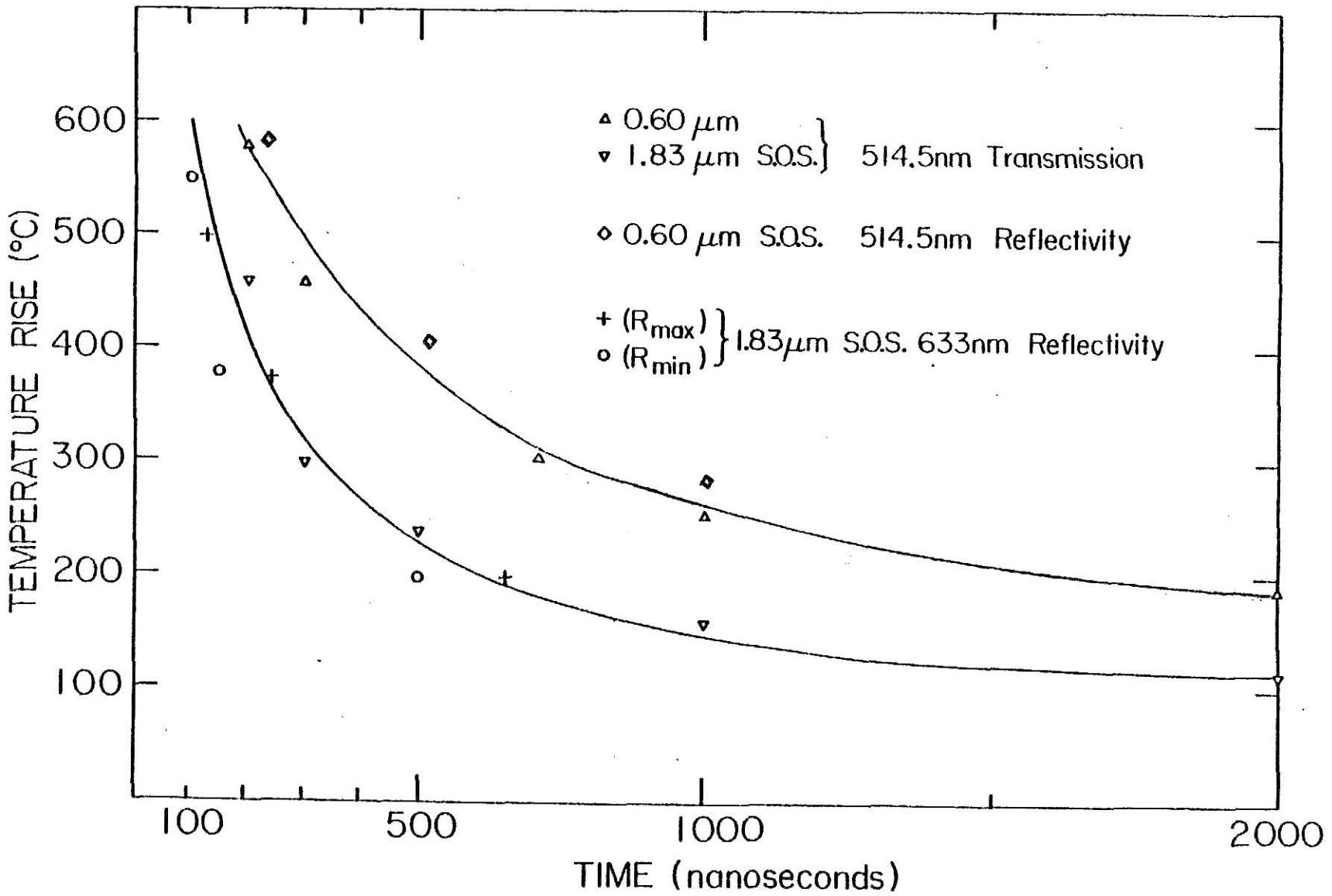
TEMPERATURE RISE (°C)
600
500
400
300
200
100
100
500
1000
2000
TIME (nanoseconds)
▲ 0.60 μm
▼ 1.83 μm S.O.S.
514.5nm Transmission
◇ 0.60 μm S.O.S. 514.5nm Reflectivity
+ (R_{max})
o (R_{min})
1.83μm S.O.S. 633nm Reflectivity

expect 2/3 of the temperature rise in 1.83 μm sample as in 0.6 μm sample. This behavior is seen in the two sets of data shown in Figure 12. If we include the data points of the 1.16 μm sample from chapter 2, we will find that they lie between the two solid curves. Thus all the results agree with one another. The striking result from this analysis is that the highest temperature we can obtain right after the enhanced reflectivity phase is less than 700°C, about one half the melting point of silicon (1410°C). The melting model cannot explain such behavior without assuming an ultra-fast cooling rate.

Another possible explanation of the band gap shift could be due to the electronic volume effect.[23] This effect results from excitation of large numbers of electrons from valence to conduction band which will cause the lattice to adjust towards a new equilibrium. In a certain range of the electron-hole pair concentration, the electronic strain in Si has a negative sign which means a lattice contraction. The volume change of the lattice has been shown by Gauster[23] to be proportional to the pressure derivative of the energy gap. Thus, it tends to shift down the band gap. By the Kramers-Kronig relation, this will also contribute to the Δ n in the interference equation in addition to the thermal heating. Therefore, the deduced temperature rise as function of time should be less than if thermal heating is considered as the only source of Δ n(T).

In concluding this chapter, we would like to say that the multiple interference effect is definitely important in the intermediate time regime. The source of this effect is mainly due to the variation in index of refraction. The effect from the thermal expansion of sample is much weaker than that from the variation in Δ n. Such variation could be induced by the lattice heating and/or the electronic volume effect.

Chapter 4

REFLECTIVITY AND TRANSMISSION IN THE HIGH REFLECTIVITY PHASE

The point we want to make is that we think most of energy remains in the electronic system and does not reach the lattice for short times (0-100 nsec). If the lattice absorbs most of the energy it should be hot enough to melt. Because the penetration depth of 485 nm pulse laser is $(1/\alpha) = 1.1$ μm, one should expect the energy to be absorbed within the first 1 μm depth. Knowing that the heat capacity of Si is not strongly temperature dependent[24] (average C_v is 0.88 J/gm/°C from room temperature to 1000°C) and the density ($D = 2.42$ gm/cm^3) for crystalline Si, we calculate the temperature rise due to depositing 0.8 J/cm^2 into the sample to be $\Delta T = (1 - R) \cdot \Delta Q/A/(D \cdot L \cdot C_v) = 1500$°C, where R is taken from the enhanced reflectivity (~0.6) and L is the absorption layer. Thus the energy deposited by the laser pulse must not be transferred to the lattice immediately but a significant fraction apparently stays in the electronic system.

If Si melts right after the laser pulse, we should not see any transmission at all due to the metallic nature[25] of molten phase of Si in which the skin depth ranges from 120Å at 1 μm to 80Å at 400 nm.[26] This means that even a 0.1 μm molten layer would require e^{-10} transmission. This is hardly observed. However, in the short-time regime, it

is not easy to distinguish the small transmission from zero. Therefore, we will look into this regime in more detail in this section.

A. Results of CW Laser Probes and Detector Response

The enhanced reflectivity during the period of 0-100 nsec. is claimed to be a strong evidence of melting by many groups because it is close to the value of molten silicon. The low transmission during this phase as probed with 633 and 514.5 nm seems to support the melting model. The relatively high transmission occuring at 1152 nm in Figures 6 (a), 7 (a), and 8 (a) appears contradictory to what the melting model would predict, since the absorption coefficient of molten silicon is extremely large ($>10^6$ cm^{-1}) even below the band edge of crystalline silicon. In the previous time, we thought this is a good point to reject the melting model. However, we found later on that there were problems with the Ge detector. One is that the fall time of pulse response is not as fast as rise time ($\sim$5 nsec), the other is that it has some residue or a tail of magnitude about 1/6 of the signal height and recovers at 150 nsec. These artifacts lead us to suspect all transmission data with 1152 nm probe.

We have investigated the Ge detector by focusing tightly the 1152 nm probe to a spot size of 63 μm in diameter at ½ power points and obtained the transmission ratio through 50 μm pinhole to be 79 percent. The results are shown in Figure 13 (a). The signal at points A has the maximum reading, one half maximum reading at points B and approximately zero at points C. At points A and on the wire, we obtained the fastest response ($<$20 nsec) of the detector. But a very slow response ($\geq$100 nsec) happened at points B. These responses are plotted in Figure 13 (b). After carefully centering the 1152 nm probe beam between two A points, we saw a

Figure 13: Investigation of Ge detector

(a) Detector geometry (top view),

(b) Response curve at two different points,

(c) 1152 nm transmission detected at good response region.

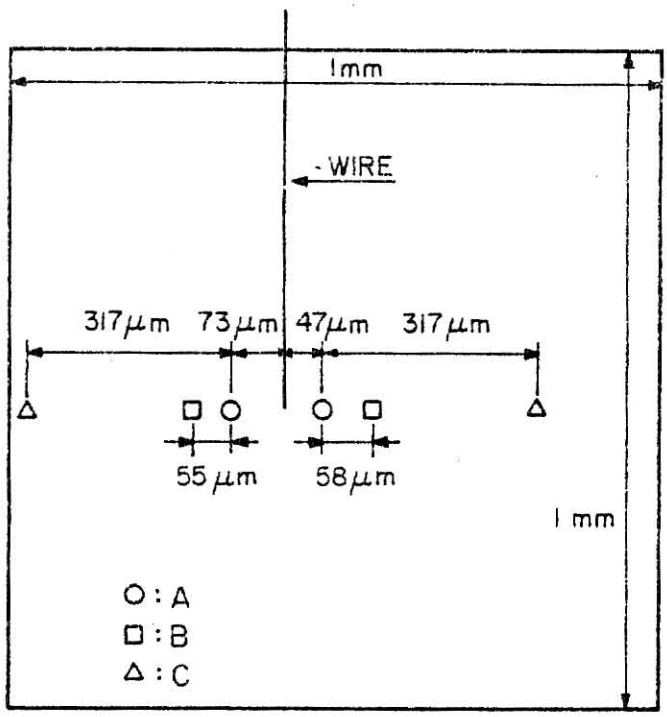
1mm
WIRE
317μm
73μm
47μm
317μm
55μm
58μm
1 mm
O : A
□ : B
△ : C

(a)

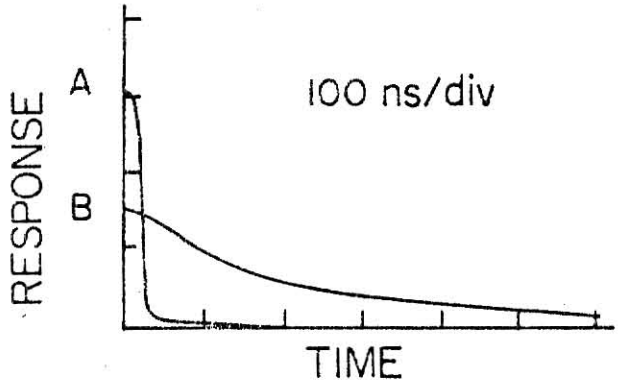
RESPONSE
A
B
100 ns/div
TIME

(b)

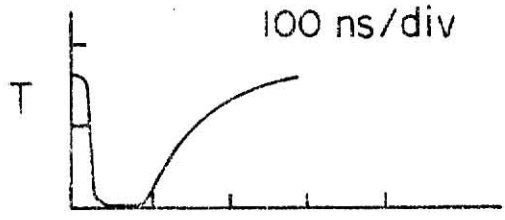
T
100 ns/div

(c)

signal almost zero during the 100 ns after the excitation pulse as shown in Figure 13 (c). Thus both reflectivity and transmission results as probed with CW lasers appear to be consistent with the melting model. In order to understand this enhanced reflectivity phase thoroughly and see whether the low transmission is in fact equivalent to the molten phase, we used the pulsed dye laser to probe the signal because it has a larger dynamic range, wide choice of wavelength and stable power. In the experimental set-up of Figure 3, the second dye laser was delayed by 25 nsec by passing through the optical delay line in order to probe the middle of the high reflectivity phase. A spatial filter was imposed in the probe right after the optical delay line to obtain a good beam profile as shown in dashed square of Figure 3. Thus the probe beam size is 55 ± 5 μm and close to what we used in the CW probe situation. However, there are factors which can affect our measurements of reflectivity and transmission such as excitation power, probe power, sample thickness, and probe wavelength. First we will discuss these factors in sequence and then apply Kramers-Kronig analysis to explain the intriguing relation between the reflectivity and the complementary transmission.

B. Power Dependence of Reflectivity and Transmission

1. Excitation Power

Usually the duration of the high reflectivity phase was used as a criterion to determine the annealing and damage thresholds. Below the annealing threshold which is 0.5 ± 0.1 J/cm^2, no enhanced reflectivity occurs. Above the damage threshold which is 1.50 ± 0.1 J/cm^2, the reflectivity never recovers to the initial value and the transmission immediately goes to almost zero with only one pulse and never recovers

either. Between annealing and damage thresholds, the duration of the enhanced reflectivity is quite stable and reproducible from 50 to 150 nsec and both reflectivity and transmission recover after the high reflectivity phase.

By examining the surface morphology of a pulsed laser-annealed ion-implanted sample under the microscope, we find that it shows a good annealing pattern when the power density is larger than 0.5 ± 10% J/cm^2. If the power density is lower than the mentioned value, the sample is partially annealed and the pattern is nonuniform. When the power density is greater than 1.5 J/cm^2, we can see a lot of puddles shown on the sample surface. Also some idea about the annealing threshold occurs to us as we find that there is a big difference in transmission ratio when power density goes below 0.6 J/cm^2. Therefore, all of the reflectivity and transmission curves were taken with power densities from 0.8 to 1.2 J/cm^2 well within the limits for good annealing.

2. Probe Power

In the beginning work, we did not pay much attention to the fact that the probe power could substantially excite the sample too. Thus the results showed quite different and inconsistent results from those of the CW probe. The transmission ratios varied randomly from 0.87 to 0.009 instead of very low ratios one would expect as shown in Figures 6, 7, 8, and 9. Therefore, we attenuated the pulse probe power by inserting a 10^{-3} filter. As long as the pulsed probe itself does not induce any change in the sample, the transmission ratios are consistent and reproducible. They range from 0.002 to 0.008 in the region of probe wavelength 405 to 770 nm. This is what we need for obtaining the spectral dependence

of the absorption coefficient.

C. Thickness Dependence of Transmission

When we did the measurements on the different thickness S.O.S. samples (2.0, 1.83, 1.16, and 0.6 μm), no matter what probe we used (CW or pulsed), the transmission and reflectivity in this 0-100 nsec period basically showed very little change from sample to sample as shown in Figure 14. But a special feature occurred while we did the same measurement on an S.O.S. wedge. This wedge was prepared by L. Rahn as described in his dissertation.[27] At sample thickness above 0.07 μm nothing was different from other samples. However, the transmission increases sharply from 0.01 to 0.57 when the thickness decreases below 0.07 μm. This leads us to suggest that the absorbing layer in silicon is confined to the first 0.07 μm approximately.

D. Spectral Dependence of Transmission

For a given transmission, the absorption coefficient is inversely proportional to the thickness of the absorbing layer. By assuming 0.07 μm as absorbing region, we are able to calculate the absorption coefficient during the high reflectivity phase. Combining CW and pulsed data, we obtain an absorption curve of spectral dependence in Figure 15. The curve shows very high absorption at 514.5 and 633 nm but falls off at 1152 nm. Because the skin depth of molten silicon has been measured by Shvarev et al.,[26] we are able to plot another curve showing the absorption coefficient of motlen silicon in the same figure. Although the two curves are close above 1.5 eV, they start to separate as the photon energy goes below 1.5 eV. If the laser annealing involves melting, this discrepancy

Figure 14: Transmission ratio measured on different thickness samples.

λ_{probe} = 450 nm

λ_{excite} = 485 nm

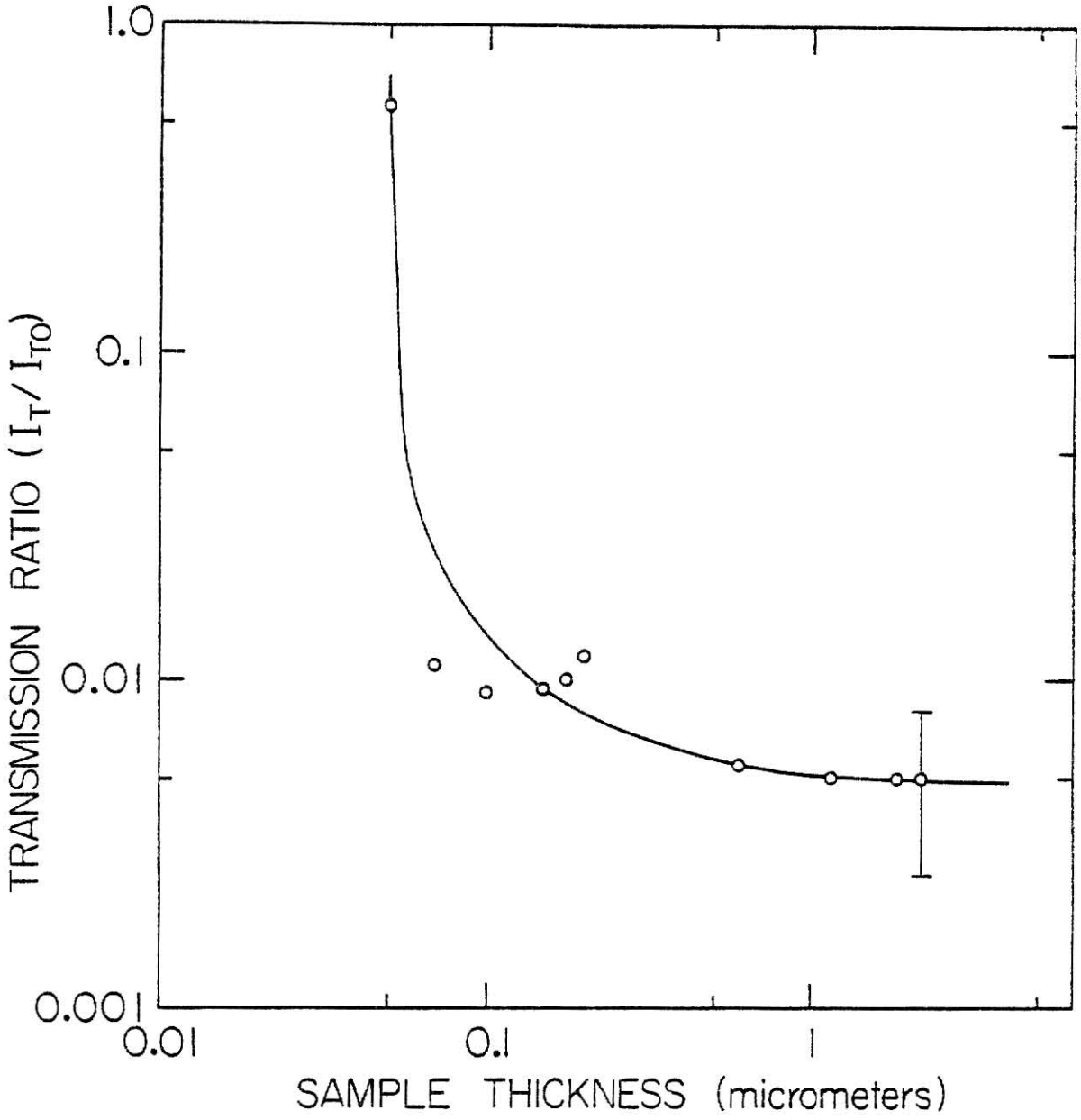
1.0
0.1
0.01
0.001
TRANSMISSION RATIO (I_T / I_{TO})
0.01
0.1
1
SAMPLE THICKNESS (micrometers)

Figure 15: Absorption curve of pulsed laser-irradiated S.O.S. during the high reflectivity phase. The dashed curve shows the absorption of molten Si. (Ref. 25.)

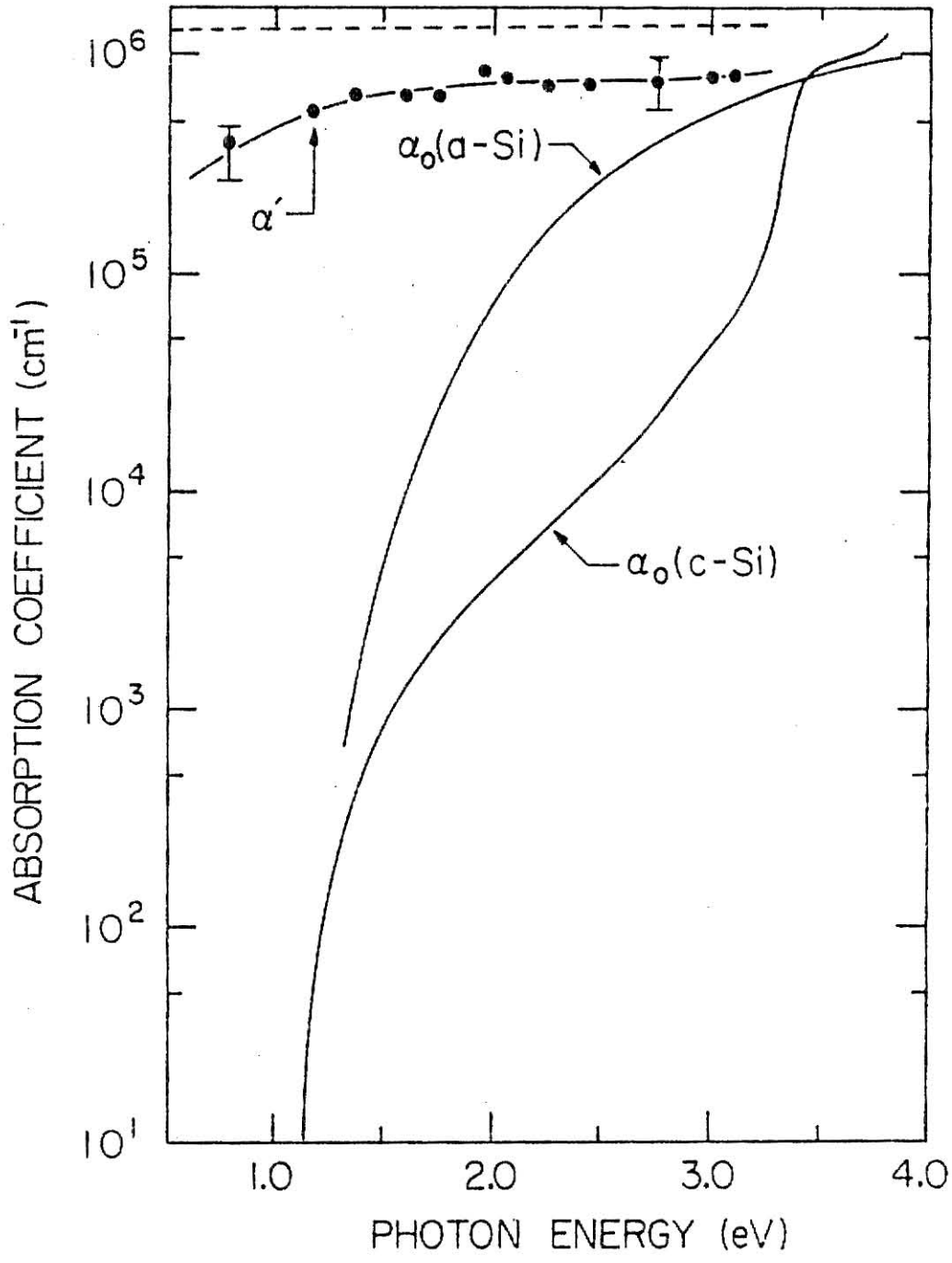
ABSORPTION COEFFICIENT (cm⁻¹)
10⁶
10⁵
10⁴
10³
10²
10¹
α₀(a-Si)
α′
α₀(c-Si)
1.0
2.0
3.0
4.0
PHOTON ENERGY (eV)

cannot be explained easily by the melting model. In the next part, we will show how the Kramers-Kronig relation with the information given in the absorption coefficient curve can give a consistent interrelationship of reflectivity and transmission.

E. Kramers-Kronig Analysis

With the knowledge of the change in the absorption coefficient over an extended frequency range, it is possible to use the Kramers-Kronig relation to calculate the corresponding change in the reflectivity because the real part and imaginary part of the index of refraction are related to each other.

$$\text{Re } n(\omega) = 1 + \frac{2}{\pi} P \int_0^\infty \frac{\text{Im } n(\omega')}{\omega' - \omega} d\omega'$$

$$\text{Im } n(\omega) = -\frac{2\omega}{\pi} P \int_0^\infty \frac{\text{Re } n(\omega') - 1}{\omega' - \omega} d\omega'$$

Where P denotes the principal part of the integral and ω is the probe angular frequency. The imaginary part of the index of refraction can be related to the absorption coefficient by multiplying by a factor of $c/2\omega$.

Thus

$$\text{Im } \Delta n(\omega) = \Delta\alpha(\omega) \times c/2\omega \quad ,$$

where c is the speed of light.

With $E = \hbar\omega$ and $E' = \hbar\omega'$, we can write down the equation for the change in the real part of the index of refraction.

$$\text{Re } \Delta n(E) = \frac{2}{\pi} P \int_0^\infty \frac{\text{Im } \Delta n(E')}{E'^2 - E^2} E' dE'$$

Then the new index of refraction will be

$$n_{new} = \text{Re } (n + \Delta n) + \text{Im } (n + \Delta n)$$

Using the simple approximation for the near normal incidence angle, the expression for the reflectivity is given by

$$R = \left(\frac{n - 1}{n + 1}\right)^2$$

Taking $\Delta\alpha = 7 \times 10^5$ cm^{-1} from 1.0 to 3.3 eV and falling smoothly to zero at 0.6 and 3.5 eV, the calculated Re $\Delta n = 2.74$ at 1152 nm, -0.5 at 633 nm and -0.97 at 514.5 nm. The change in the imaginary part of the index of refraction can be found directly from absorption curve in Figure 15 to be 6.4 at 1152 nm, 3.5 at 633 nm, and 2.87 at 514.5 nm. Thus the new reflectivity is given by

$$R_{new} = \frac{[1 - \text{Re } (n + \Delta n)]^2 + \text{Im } (n + \Delta n)^2}{[1 + \text{Re } (n + \Delta n)]^2 + \text{Im } (n + \Delta n)^2}$$

Since Im (Δn) is much greater than Im (n), the calculated R_{new} is 0.73 at 1152 nm, 0.57 at 633 nm, and 0.51 at 514.5 nm. They are all close to the measured values of 0.6 ± 0.1. The small discrepancy might be explained by the extrapolations of $\Delta\alpha$ as a simple function of photon energy. However, we also did a calculation by assuming the flat absorption curve down to 0 eV which is similar to the molten situation. The calculated value for the enhanced reflectivity is 0.83 at 1152 nm. This is not consistent with the experimental result which is about 0.6.

Therefore, the Kramers-Kronig analysis provides as independent experimental evidence of self confinement, and thus strengthens our belief in some induced, confined phase during pulsed laser annealing which is different from the normal molten phase of silicon.

Chapter 5

DISCUSSION AND CONCLUSION

The enhanced reflectivity during the high reflectivity phase (70 - 100 nsec in duration) can be explained by the high absorption by using the Kramers-Kronig relations and an assumption of 0.07 μm for the absorbing layer thickness. This assumption is based on the measured reflectivity and transmission and thus invokes an idea of self-confinement in the non-thermal annealing model.

After the high reflectivity phase, when the multiple interference effect becomes important, the highest temperature we can infer from the reflectivity data is less than 700°C. As time elapses, the thermalization between the electronic system and the lattice is reached by 1 μsec where temperature is only 250 ± 20°C. This is far below the melting point of silicon.

Although many phenomena in pulsed-laser annealing can be understood in this experiment by the non-thermal (induced self-confinement) annealing model, an accurate theory is still not built up yet. There are many phenomena such as cell formation, impurity segregation, electrical conductivity, diffusion rate, enhanced reflectivity, low lattice temperature, and the existence of a confined region which are not yet fully explained.

Therefore, it is obvious that more work needs to be done to re-

solve the controversy of the mechanism of pulsed-laser annealing, for instance how to measure the regrowth velocity, the highly excited layer and even the decay time of hot carriers.

APPENDICES

The programs for computing the multiple interference and Kramers-Kronig relation follow. One can use the programs in Appendices 1 and 2 to calculate the multiple reflection and transmission at 514.5 and 633 nm respectively with respect to temperature. The input parameters are sample thickness, probe wavelength, index of refraction at room temperature and number of data points. The temperature interval between data points is 20°C.

In Appendix 3, for a given absorption curve, one may divide it into five photon energy regions. By entering the x-y coordinates of region boundaries and probe photon energy, the K-K analysis program can be used to calculate the real part of the index of refraction.

```
MULIN1.FOR
      INTEGER DBLK(4),WCODE,R(512),T(512),TEMP(512)
      LOGICAL*1 NAME1(12),NAME2(12),ANS
C     MULTIPLE INTERFERENCE EFFECT DUE TO THE TEMPERATURE
C     DEPENDENCE OF INDEX OF REFRACTION AND ABSORPTION COEFF.

      CALL PRINT('ENTER SAMPLE THICKNESS IN MICRON')
      ACCEPT 1,Z
1     FORMAT (F10.6)
      CALL PRINT('ENTER PROBE WAVELENGTH IN MICRON')
      ACCEPT 1,W
      CALL PRINT('ENTER INDEX OF REFRACTION AT ROOM TEMP.')
      ACCEPT 1,A
      CALL PRINT ('ENTER NUMBER OF DATA POINTS')
      ACCEPT 10,NO
10    FORMAT(I3)
      DO 2 J=1,NO
      PI=4*ATAN(1.)
      TEMP(J)=20.*J
      C1=0.0028*TEMP(J)
      E1=EXP(C1)
      C2=-0.9*Z*E1
      E=EXP(C2)
      D1=4.*A*Z*PI/W
      D2=4.*0.000546*Z*TEMP(J)*PI/W
      D=D1+D2
      CS=COS(D)
      RL=-0.615
      T1=0.385
      T2=1.615
      R1=RL*RL
      TC=T1*T2
      RC=-R1+TC
      X2=0.423*0.423*R1*E*E
      X3=2.*0.423*RL*E*CS
      X=1.+X2+X3
      T(J)=1000.*1.423*T1*E/X
      R2=0.423*0.423*RC*RC*E*E
      R3=2.*0.423*RL*RC*E*CS
2     R(J)=1000.*(R1+R2-R3)/X
      TYPE 3,(R(J),T(J),TEMP(J),J=1,NO)
3     FORMAT(' ','R='I6,5X,'T='I6,5X,'TEMP='I6/)
      CALL PRINT('WANT TO WRITE DATA ON DISK?')
      ACCEPT 21,ANS
21    FORMAT(A1)
      IF(ANS.NE.'Y') STOP
      CALL GTLIN(NAME1,'ENTER REFLECTIVITY FILE NAME')
      CALL IRAD50(12,NAME1,DBLK)
      IFET=IFETCH(DBLK)
      IEN=IENTER(2,DBLK,-1)
      M=0
      WCODE=IWRITW(NO,R,M,2)
      CALL CLOSEC(2)
      CALL GTLIN(NAME2,'ENTER TRANSMISSION FILE NAME')
      CALL IRAD50(12,NAME2,DBLK)
      IFET=IFETCH(DBLK)
      IEN=IENTER(2,DBLK,-1)
      M=0
      WCODE=IWRITW(NO,T,M,2)
      CALL CLOSEC(2)
      STOP
      END
```

```
MULIN2.FOR
      INTEGER DBLK(4),WCODE,R(512),T(512),TEMP(512)
      LOGICAL*1 NAME1(12),NAME2(12),ANS
C     MULTIPLE INTERFERENCE EFFECT DUE TO THE TEMPERATURE
C     DEPENDENCE OF INDEX OF REFRACTION AND ABSORPTION COEFF.

      CALL PRINT('ENTER SAMPLE THICKNESS IN MICRON')
      ACCEPT 1,Z
1     FORMAT (F10.6)
      CALL PRINT('ENTER PROBE WAVELENGTH IN MICRON')
      ACCEPT 1,W
      CALL PRINT('ENTER INDEX OF REFRACTION AT ROOM TEMP.')
      ACCEPT 1,A
      CALL PRINT ('ENTER NUMBER OF DATA POINTS')
      ACCEPT 10,NO
10    FORMAT(I3)
      DO 2 J=1,NO
      PI=4*ATAN(1.)
      TEMP(J)=20.*J
      C1=0.00258*TEMP(J)
      E1=EXP(C1)
      C2=-0.32*Z*E1
      E=EXP(C2)
      D1=4.*A*Z*PI/W
      D2=4.*0.00047*Z*TEMP(J)*PI/W
      D=D1+D2
      CS=COS(D)
      RL=-0.588
      T1=0.412
      T2=1.588
      T3=1.26
      R1=RL*RL
      TC=T1*T2
      RC=-R1+TC
      X2=0.367*0.367*R1*E*E
      X3=2.*0.367*RL*E*CS
      X=1.+X2+X3
      T(J)=1000.*1.38*1.38*T1*T1*E/X
      R2=0.367*0.367*RC*RC*E*E
      R3=2.*0.367*RL*RC*E*CS
2     R(J)=1000.*(R1+R2-R3)/X
      TYPE 3,(R(J),T(J),TEMP(J),J=1,NO)
3     FORMAT(' ','R=',I6,5X,'T=',I6,5X,'TEMP=',I6/)
      CALL PRINT('WANT TO WRITE DATA ON DISK?')
      ACCEPT 21,ANS
21    FORMAT(A1)
      IF(ANS.NE.'Y') STOP
      CALL GTLIN(NAME1,'ENTER REFLECTIVITY FILE NAME')
      CALL IRAD50(12,NAME1,DBLK)
      IFET=IFETCH(DBLK)
      IEN=IENTER(2,DBLK,-1)
      M=0
      WCODE=IWRITW(NO,R,M,2)
      CALL CLOSEC(2)
      CALL GTLIN(NAME2,'ENTER TRANSMISSION FILE NAME')
      CALL IRAD50(12,NAME2,DBLK)
      IFET=IFETCH(DBLK)
      IEN=IENTER(2,DBLK,-1)
      M=0
      WCODE=IWRITW(NO,T,M,2)
      CALL CLOSEC(2)
      STOP
      END
```

KKANAL.FOR

```
      DIMENSION SLOPE(5),YINT(5),XCOOR(6),YCOOR(6),Z1(5),Z2(5)
       REAL NREAL
       CALL PRINT('TYPE IN NO OF REGIONS')
       ACCEPT 1,IREGN
1      FORMAT(I1)
       CALL PRINT('ENTER X-COORDINATES')
       DO 2 I=1,IREGN+1
2      ACCEPT 3,XCOOR(I)
       CALL PRINT('ENTER Y-COORDINATES')
       DO 4 I=1,IREGN+1
4      ACCEPT 3,YCOOR(I)
3      FORMAT(E15.7)
       DO 5 I=1,IREGN
       SLOPE(I)=(YCOOR(I+1)-YCOOR(I))/(XCOOR(I+1)-XCOOR(I))
       YINT(I)=YCOOR(I)-SLOPE(I)*XCOOR(I)
5      TYPE 8,SLOPE(I),YINT(I)
8      FORMAT(' ',E15.7,1X,E15.7,/)
9      CALL PRINT('TYPE IN PROBE PHOTON ENERGY')
       ACCEPT 3,PROBE
       PI=4.*ATAN(1.)
       HBAR=4.1356E-15/2./PI
       C=3.0E10
       SUM=0.
       DO 6 I=1,IREGN
       Z1(I)=SLOPE(I)*PROBE*(ALOG(ABS((XCOOR(I+1)-PROBE)*(XCOOR(I
       11)+PROBE)/(XCOOR(I)-PROBE)/(XCOOR(I)+PROBE))))
       Z2(I)=YINT(I)*(ALOG(ABS((XCOOR(I+1)-PROBE)*(XCOOR(I)+PROBE
       1/(XCOOR(I+1)+PROBE)/(XCOOR(I)-PROBE))))
       SUM=SUM+Z1(I)+Z2(I)
6      TYPE 8,Z1(I),Z2(I)
       NREAL=SUM*C*HBAR/2./PI/PROBE
       TYPE 7,NREAL
7      FORMAT(' ','THE RESULT IS ',F10.5,/)
       GOTO 9
       END
```

REFERENCES

1. J. W. Mayer, L. Eriksson, and J. A. Davies, Ion Implantation in Semiconductors: Silicon and Germanium, Academic Press, NY (1970).

2. C. W. White, J. Narayan, and R. T. Young, Science 461, 204 (1979).

3. I. B. Khaibullin, E. I. Shtyrkov, M. M. Zaripov, and M. F. Galyautdinov Deposited Paper No. 2061-74 (in Russian) VINITI, Moscow (1974).

4. D. H. Auston, J. A. Golovchenko, A. L. Simons, and C. M. Surko, Appl. Phys. Lett. 34(11), 777 (1979), and reference therein, D. H. Auston, C. M. Surko, T. N. C. Venkatesan, R. E. Slusher, and J. A. Golovchenko, Appl. Phys. Lett. 33(5), 437 (1978).

5. J. A. Van Vechten, R. Tsu, F. W. Saris, and D. Hoonhout, Phys. Lett. 74A, 417 (1979). J. A. Van Vechten, R. Tsu, and F. W. Saris, Phys. Lett. 74A, 422 (1979). M. Wautelet, and J. A. Van Vechten, Phys. Rev. B23, (1981). J. A. Van Vechten, and A. D. Compaan, Solid State Comm. Vol 39, pp 867-873 (1981), and reference therein.

6. I. B. Khaibullin, E. I. Shtyrkov, M. M. Zaripov, M. F. Galyautdinov, and G. G. Zakirov, Sov. Phys. Semicond. Vol. 11, No. 2, 190 (1977). R. F. Wood, Appl. Phys. Lett. 37(3) 302, (1980).

7. J. Narayan, J. Fletcher, C. W. White, and W. H. Christie, J. Appl. Phys. 52(12), 7121 (1981).

8. C. W. White, S. R. Wilson, B. R. Appleton, and J. Narayan, in Laser and Electron Beam Processing of Materials edited by C. W. White and P. S. Peercy, pp 124-129, Academic Press (1980).

9. H. W. Lo, and A. D. Compaan, Phys. Rev. Lett. 44, 1604 (1980).

10. M. Yamada, K. Yamazaki, H. Kotani, K. Yamamoto, and K. Abe, in "Laser and Electron-Beam Solid Interactions and Materials Processing" edited by J. F. Gibbons, L. D. Hess, and T. W. Sigman (North-Holland, New York 1981), p 503.

11. M. Yamada, H. Kotani, K. Yamazaki, K. Yamamoto, and K. Abe, in proceedings of the Fifteenth International Conference on Physics of Semiconductors, Kyoto, Japan, Sep. 1-6, 1980.

12. J. A. Van Vechten, R. Tsu, F. W. Saris, and D. Hoonhout, Phys. Lett. 74A 417 (1979).

13. R. Tsu, J. E. Baglin, T. Y. Fan, and R. J. von Gutfeld, in "Laser and Electron Beam Processing of Electronic Materials" edited by C. L. Anderson, G. K. Celler, and G. A. Rozgonyi. (Electrochemical Society, Princeton, 1980), p 382.

14. D. Hoonhout, and F. W. Saris, Phys. Lett. 74A, 253 (1979).

15. P. Baeri, S. U. Campisano, G. Foti, and E. Rimini, Phys. Rev. Lett. 41, 1246 (1978).

16. E. J. Yoffa, Appl. Phys. Lett. 36(1), 37 (1980).

17. M. C. Lee, H. W. Lo, A. Aydinli, and A. Compaan, Appl. Phys. Lett. 38(7), 499 (1981).

18. A. Aydinli, H. W. Lo, M. C. Lee, and A. Compaan, Phys. Rev. Lett. Vol. 46 No. 25, 1640 (1981).

19. G. E. Jellison, and F. A. Modine (submitted for publication).

20. K. Murakami, K. Takita, and K. Masuda, Japanese J. Appl. Phys. Vol 20, No. 12, Dec. (1981). H. A. Weakliem and D. Redfield, J. Appl. Phys. 59(3) 1491, (1979).

21. H. Ibach, Phys. Stat. Sol. 31, 625 (1969).

22. The results of Ref. 19 are $c = 2.2 \times 10^{-3}/^{o}c$ at 633 nm and $c = 2.3 \times 10^{-3}/^{o}c$ at 514.5 nm. The difference between theirs and ours is within experimental error.

23. W. B. Gauster, and D. H. Habing, Phys. Rev. Lett. Vol 18, No 24, 1058 (1967). W. B. Gauster, Phys. Rev. Vol 187, No 3, 1035 (1969). J. A. Van Vechten, Japanese J. Appl. Phys. 21 L125, (1982).

24. Selected Values of Thermodynamic Properties of the Elements, edited by R. T. Hultgren (American Society for Metals, Metals Park, Ohio, 1973).

25. J. M. Ziman, Principles of the Theory of Solids, Cambridge (1965) p 240.

26. K. M. Shvarev, B. A. Baum, and P. V. Gel'd, Fiz. Tverd. Tela 16, 3246 (1974).

27. L. A. Rahn, Ph.D. dissertation, "The Raman Spectra of Some Imperfect Crystals of Silicon," p 67, Kansas State University (1973).

TIME-RESOLVED TRANSMISSION AND REFLECTIVITY STUDIES OF PULSED-LASER IRRADIATED SILICON-ON-SAPPHIRE

by

MING-CHIH LEE

B. S., Chung Yuan Christian College of
Science and Engineering, 1975

AN ABSTRACT OF A MASTER'S THESIS

submitted in partial fulfillment of the

requirements for the degree

MASTER OF SCIENCE

Department of Physics

KANSAS STATE UNIVERSITY
Manhattan, Kansas

1982

ABSTRACT

The time-resolved transmission and reflectivity of pulsed-laser irradiated silicon-on-sapphire have been studied under pulsed-laser annealing conditions. In the time period of ∿100 nanoseconds to tens of microseconds after the pulse, both the reflectivity and transmission show oscillatory behavior which is caused by a multiple interference effect. Using the well-known multiple reflection and transmission equations, we can simulate this behavior by putting in the temperature-dependent parameters (absorption coefficient, index of refraction, and sample thickness) and thus obtain the temperature as a function of time. The highest temperature rise we obtain after the enhanced reflectivity is less than 700°C. During the first 100 nanoseconds, we see a depressed transmission of the same period as the enhanced reflectivity phase. By applying the Kramers-Kronig relations, we verify that the enhanced reflectivity is mainly due to the absorption increase. Our experimental results appear to be in contradiction to the normal melting model as described in the literature unless an ultrafast cooling rate is assumed.